

**DEVELOPMENT OF ZIRCONIA CERAMIC  
BASED FEEDSTOCK FOR ADDITIVE  
MANUFACTURING TECHNOLOGY**

**WONG ZONG QI**

**UNIVERSITI TUNKU ABDUL RAHMAN**

**DEVELOPMENT OF ZIRCONIA CERAMIC BASED FEEDSTOCK  
FOR ADDITIVE MANUFACTURING TECHNOLOGY**

**WONG ZONG QI**


**A project report submitted in partial fulfilment of the  
requirements for the award of Bachelor of Mechanical Engineering with  
Honours**

**Lee Kong Chian Faculty of Engineering and Science  
Universiti Tunku Abdul Rahman**

**May 2023**

**DECLARATION**

I hereby declare that this project report is based on my original work except for citations and quotations which have been duly acknowledged. I also declare that it has not been previously and concurrently submitted for any other degree or award at UTAR or other institutions.

Signature :  \_\_\_\_\_

Name : Wong Zong Qi

ID No. : 1803862

Date : 22/05/2023

**APPROVAL FOR SUBMISSION**

I certify that this project report entitled “**DEVELOPMENT OF ZIRCONIA CERAMIC BASED FEEDSTOCK FOR ADDITIVE MANUFACTURING TECHNOLOGY**” was prepared by **WONG ZONG QI** has met the required standard for submission in partial fulfilment of the requirements for the award of Bachelor of Engineering (Honours) Mechanical Engineering at Universiti Tunku Abdul Rahman.

Approved by,

Signature

:



Supervisor

:

Ting Chen Hunt

Date

:

22/05/2023

Signature

:

Co-Supervisor

:

Date

:

The copyright of this report belongs to the author under the terms of the copyright Act 1987 as qualified by Intellectual Property Policy of Universiti Tunku Abdul Rahman. Due acknowledgement shall always be made of the use of any material contained in, or derived from, this report.

© 2023, Wong Zong Qi. All right reserved.

## ACKNOWLEDGEMENTS

I would like to express my sincere gratitude to my research supervisor, Dr. Ting Chen Hunt for his crucial guidance, patience, and counsel during the research's development. His enthusiasm, vision and motivation had greatly influenced me. He had shown me how to conduct the study and how to present the results. Working with and learning from him was an immense pleasure and privilege.

Besides, I would like to thank my senior, Ignatius Lim Yuze for his advice and instruction on the operation of equipment and advice. His guidance and advice had help me to conduct my preparation and conduction of lab work correctly. His friendship, comprehension and amazing sense of humour added to the enjoyment of the research process.

Moreover, I would like to thank Universiti Tunku Abdul Rahman and Tunku Abdul Rahman University of Management and Technology for granted me the access of using all the necessary lab equipment to conduct my research. All the application were granted efficient and fast without any restrictions which made the research proceed as planned.

In addition, I would want to express my heartfelt appreciation to everyone who has supported me along the way in this final year project. I am thankful to my friends and family who had support and encouraged me. This work would not been possible without their assistance.

## ABSTRACT

Additive Manufacturing (AM) also known as 3D printing, has become a hot topic of research in recent years. It offers several advantages over traditional manufacturing methods, such as flexibility, waste reduction and dimensional accuracy. However, there is limited research on the rheological and thermal properties of Zirconia-based feedstock with varying solid loading. Additionally, there is a lack of studies exploring the mechanical properties of sintered specimens with different chemical solvent debinding methods and ceramic solid loading. Furthermore, the extent to which mechanical properties are affected by altering printing parameters remains uncertain. In this research, the pellet feedstock will consist of zirconia doped with 3 mol% yttria as the ceramic based material. It was mixed with low-density polyethylene (LDPE), paraffin wax (PW) and stearic acid (SA) as the binders for fused deposition modelling (FDM) 3D printer. The feedstock with different solid loading percentages, which are 60 vol%, 65 vol% and 68 vol% were analysed. Additionally, the feedstocks maintained a constant ratio of LDPE:PW=40:60 and SA with a constant rate of  $2.27 \text{ mg/m}^2$  for total specific surface area of zirconia. The feedstock undergone a total of four processing steps to obtain a dense and robust zirconia part: i) Printing, ii) Solvent debinding, iii) Thermal debinding, and iv) Sintering. This research aim to analyze comprehensive set of properties, including i) Rheological properties of the feedstock ii) Thermal properties iii) Effect of solid loading, raster angle, build orientation and solvent used in solvent debinding on the flexural/ tensile/ compressive strength, Vickers hardness, density, shrinkage behaviour and the micro/macro structure of the sintered sample. The viscosity of the feedstocks decreased as the temperature increased, exhibited shear thinning behaviour. Besides, PW and LDPE began to decompose at  $140^\circ\text{C}$  and  $400^\circ\text{C}$  respectively. The sintered samples exhibited an average relative density ranging from 96.36 % to 97.33 %. The maximum average ultimate flexural, tensile and compressive strength of the sintered specimen were 29.53 MPa, 115.12 MPa, and 847.5 8MPa respectively. Lastly, the maximum Vickers hardness of the sintered specimen was 1228.84 HV.

## TABLE OF CONTENTS

<b>DECLARATION</b>		<b>i</b>
<b>APPROVAL FOR SUBMISSION</b>		<b>ii</b>
<b>ACKNOWLEDGEMENTS</b>		<b>iv</b>
<b>ABSTRACT</b>		<b>v</b>
<b>TABLE OF CONTENTS</b>		<b>vi</b>
<b>LIST OF TABLES</b>		<b>ix</b>
<b>LIST OF FIGURES</b>		<b>x</b>
<b>LIST OF SYMBOLS / ABBREVIATIONS</b>		<b>xii</b>
<b>LIST OF APPENDICES</b>		<b>xiii</b>
 <b>CHAPTER</b>		
<b>1</b>	<b>INTRODUCTION</b>	<b>1</b>
1.1	Background	1
1.2	Importance of the Study	2
1.3	Problem Statement	3
1.4	Aim and Objectives	3
1.5	Scope and Limitation of the Study	4
<b>2</b>	<b>LITERATURE REVIEW</b>	<b>5</b>
2.1	Introduction	5
2.2	Ceramic-Based Additive Manufacturing Overview	5
2.3	Thermogravimetric Analysis	9
2.4	Rheological Properties and Mechanical Testing	9
2.4.1	Viscosity and Linear Viscoelastic Range	10
2.4.2	Tensile Test	13
2.4.3	Flexural Test	14
2.4.4	Compressive Test	15
2.4.5	Hardness Test	16



2.5	Printing Parameter	17
2.5.1	Build Orientation	17
2.5.2	Layer Height	18
2.5.3	Raster Angle	19
2.5.4	Air Gap	19
2.5.5	Infill Density and Pattern	20
2.5.6	Extrusion Temperature	20
2.5.7	Nozzle Diameter and Raster Width	21
2.6	Type of Solvent in Solvent Debinding	21
2.7	Scanning Electron Microscope	23
2.8	X-ray Diffraction analysis	23
2.9	Summary of Literature Review	24
<b>3</b>	<b>METHODOLOGY AND WORK PLAN</b>	<b>26</b>
3.1	Introduction	26
3.2	Feedstock Preparation	26
3.3	TGA	28
3.4	Rheology Testing	28
3.4.1	Viscosity	28
3.4.2	Oscillatory Strain Sweep	29
3.5	Specimen Preparation	29
3.5.1	Printing of Green Body	29
3.5.2	Debinding	30
3.5.3	Sintering	31
3.6	Density Test	32
3.7	Scanning Electron Microscope	33
3.8	X-ray Diffraction Analysis	33
3.9	Mechanical Testing	34
3.9.1	Tensile Testing	34
3.9.2	Flexural Testing	35
3.9.3	Compressive Testing	36
3.9.4	Hardness Testing	37
3.10	Work Breakdown Structure	38
<b>4</b>	<b>RESULTS AND DISCUSSION</b>	<b>39</b>
4.1	Introduction	39

4.2	Thermal Properties of Feedstock	39
4.3	Rheological Properties of Feedstock	41
4.3.1	Viscosity Test	41
4.3.2	Oscillatory strain sweep	43
4.4	Scanning Electron Microscope	44
4.5	X-ray Diffraction Analysis	46
4.6	Physical Properties of Sintered Specimen	48
4.6.1	Shrinkage of Sintered Specimen	48
4.6.2	Weight Loss of Solvent Debound and Sintered Specimen	49
4.6.3	Density of Sintered Specimen	50
4.7	Mechanical Properties of Sintered Specimen	52
4.7.1	Tensile Strength	53
4.7.2	Flexural strength	54
4.7.3	Compressive Strength	55
4.7.4	Vickers Hardness	56
4.8	Summary of Results	58
<b>5</b>	<b>CONCLUSIONS AND RECOMMENDATIONS</b>	<b>61</b>
5.1	Conclusions	61
5.2	Recommendations for future work	62
5.2.1	Prepare More Testing Sample for Tensile Test	62
5.2.2	Shorten The Time for Thermal Debinding	62
5.2.3	Using of Composite Backbone Binder	62
5.2.4	Explore More Solvent for Solvent Debinding	62
	<b>REFERENCES</b>	<b>63</b>
	<b>APPENDICES</b>	<b>65</b>

**LIST OF TABLES**

Table 3.1:	Variable of Printing Parameter	30
Table 3.2:	Type of Specimen	34
Table 4.1:	Table of average grain size of sintered specimen with different solid loading and solvent	46
Table 4.2 :	Type of specimens	52
Table 4.3:	Table of tensile test results with different sintered specimens	53
Table 4.4:	Table of Different Feedstock's Properties	58
Table 4.5:	Table of Different Type of Sintered Specimen's Grain Size	59
Table 4.6:	Table of Different Type of Sintered Specimen's Physical Properties	59
Table 4.7:	Table of Different Type of Sintered Specimen's Mechanical Properties	60

## LIST OF FIGURES

Figure 2.1:	Processes of Multi-step AM	8
Figure 2.2:	Viscosity Behaviour of Newtonian and non-Newtonian Fluid (RheoSence, 2022)	11
Figure 2.3:	Result of Oscillatory Strain Sweep (Huang, et al. 2021)	12
Figure 2.4:	Shear Yield Strain (Huang, et al. 2021)	12
Figure 2.5:	Dog Bone Shape Sample for Tensile Test	14
Figure 2.6:	Three-point Bending Test	15
Figure 2.7:	Build Orientation	18
Figure 2.8:	Layer Height	18
Figure 2.9:	Raster Angle of Printed Sample (Huang, et al., 2021)	19
Figure 2.10:	Infill Pattern	20
Figure 2.11:	Raster Width	21
Figure 2.12:	Phase diagram of yttria-stabilized zirconia (Witz et al., 2007)	24
Figure 3.1:	Graph of thermal debind and pre-sintering profile	31
Figure 3.2:	Graph of sintering profile	32
Figure 3.3:	Dimension of Dog Bone Shape Sample for Tensile Test	35
Figure 3.4:	Work Breakdown Structure of Project	38
Figure 4.1:	Thermal properties of 60 vol% zirconia feedstock	40
Figure 4.2:	Thermal properties of 65 vol% zirconia feedstock	40
Figure 4.3:	Thermal properties of 68 vol% zirconia feedstock	41
Figure 4.4:	Graph of Viscosity Test Result of 60 vol% Solid Loading	42
Figure 4.5:	Graph of Viscosity Test Result of 65 vol% Solid Loading	42
Figure 4.6:	Graph of Viscosity Test Result of 68 vol% Solid Loading	42

Figure 4.7:	Graph of Oscillatory Strain Sweep of 60 vol% Solid Loading	43
Figure 4.8:	Graph of Oscillatory Strain Sweep of 65 vol% Solid Loading	44
Figure 4.9:	Graph of Oscillatory Strain Sweep of 68 vol% Solid Loading	44
Figure 4.10:	SEM morphology of polished and thermal etched sintered specimen under different magnification. (a) 60 vol%, cyclohexane (b) 65 vol%, cyclohexane (c) 68 vol%, cyclohexane (d) 65 vol%, Turpentine (e) 65 vol%, N-heptane	45
Figure 4.11:	XRD pattern of sintered zirconia with different solid loading and solvent debind	47
Figure 4.12:	Phase diagram of yttria-stabilized zirconia at 3 mol% yttria, 1500 °C (Witz et al., 2007)	47
Figure 4.13:	Bar chart of dimension shrinkage of sintered sample with different solid loading and debinding solvent	49
Figure 4.14:	Bar chart of weight loss of sintered specimen with different solid loading and debinding solvent	50
Figure 4.15:	Bar chart of bulk density of sintered samples with different solid loading and debinding solvent	51
Figure 4.16:	Bar chart of relative density of sintered specimen with different solid loading and debinding solvent	52
Figure 4.17:	Bar chart of flexural strength of sintered specimen with different solid loading, debinding solvent and raster angle	55
Figure 4.18:	Bar chart of compressive strength of sintered specimen with different solid loading, debinding solvent and build-orientation	56
Figure 4.19:	Bar chart of Vickers hardness of sintered specimen with different solid loading and debinding solvent	57

**LIST OF SYMBOLS / ABBREVIATIONS**

$m$	Mass
$\rho$	Density
vol%	Volume percentage
$V$	Volume
wt%	Weightage
°C	Degree Celsius
$\rho_b$	Bulk density
$\rho_{fl@27^\circ C}$	Density of immersion fluid at 27 °C
$\rho_{ZrO_2}$	Density of zirconia
$W_a$	Sample's weight in air
$W_{fl}$	Sample's weight in immersion fluid
$F$	Force
$t$	Sample's thickness
$A$	Cross section area
$HV$	Vickers number
Pa	Pascal
s	Second
$G'$	Storage modulus
$G''$	Loss modulus
AM	Additive Manufacturing
FDM	Fused deposition Modelling
PE	Polyethylene
LDPE	Low density polyethylene
PW	Paraffin wax
SA	Stearic acid
STL	Standard Triangle Language/ Standard Tessellation Language
ASTM	American Society for Testing and Materials
TGA	Thermogravimetric analysis
ISO	International Organization for Standardization
SEM	Scanning Electron Microscope
XRD	X-ray Diffraction Analysis

**LIST OF APPENDICES**

Appendix A: Specification of Zirconia Powder	65
Appendix B: Feedstock Preparation	66
Appendix C: Detail Slicer Setting for Specimen Printing	67
Appendix D: 3D Printer	68
Appendix E: Specimen for SEM	69
Appendix F: Printed, Debound and Sintered Sample	70
Appendix G: Cracking of Sample	72
Appendix H: Fracture of Sample After Tensile Test	73
Appendix I: Tensile Test Specimen with Aluminum Plate	74
Appendix J: Fracture of Sample After Three Point Bend Test	75
Appendix K: Delamination of Compressive Sample	76
Appendix L: Diamond Indent of Vickers Hardness Test	77

## CHAPTER 1

### INTRODUCTION

#### 1.1 Background

In the early stages of additive manufacturing (AM), the primary application of this technology was rapid prototyping. However, extensive research had been conducted across various industrial sectors, including aerospace, civil, and biomedical fields, to expand the application of AM (Liu, Lei, and Xing, 2019). This increased interest in AM can be attributed to several advantages it offers over traditional manufacturing methods, such as dimensional accuracy, flexibility of design, and cost-effectiveness (Shaik, Schuster, and Shaik, 2021). Despite these benefits, there are certain limitations that hinder AM from completely replacing traditional technique for fully functional mechanical components. These limitations include limited material selection, restricted build size, and long post-processing time. These factors contribute to the continued coexistence of AM and traditional methods in various manufacturing applications (Solomon, Sevvel, and Gunasekaran, 2021).

Fused deposition modelling (FDM) is a notable method in AM due to its effectiveness in prototype printing (Shaik, Schuster, and Shaik, 2021). Within AM, ceramic materials have gained attention as potential choices for FDM due to their unique characteristics. Among ceramics, Zirconium dioxide, or Zirconia, stands out because of its exceptional properties such as thermal and electrical insulation, excellent wear and corrosion resistance, and high-temperature strength. (Faes et al., 2015). To utilize ceramics in FDM-based AM, thermoplastic binders are synthesized with ceramic powders prior to the printing process. These binders serve to overcome the high melting point and brittle nature of ceramics. The thermoplastic binders consist of plasticizers, backbone binders, and additives, and they fulfill specific requirements of the FDM process. They reduce the viscosity of the composite, enhance adhesive and cohesive forces, and act as a surfactant for the composite material. The feedstock is then extruded through the hot printer's nozzle to produce the green part. After the green part is printed, the binder's system needs to be removed through a debinding process to obtain a debound part. This debinding process typically



involves two steps: solvent debinding and thermal debinding. In solvent debinding, chemical solvents are used to dissolve and remove the binder from the green part. The thermal debinding step involves subjecting the part to elevated temperatures to further eliminate the remaining binder components. Finally, the debound part undergoes high-temperature sintering to achieve densification and strength, resulting in a robust and dense ceramic part. This sintering process involves heating the part to a temperature below its melting point but high enough to enable particle rearrangement and bonding. The end result is a finished ceramic component ready for use. (Huang et al., 2021)

In addition, various printing parameters, such as build orientation, raster angle, layer width, and layer height, can be adjusted to achieve the desired physical and mechanical properties of the printed part. However, it is important to note that due to the unique properties of ceramic materials, the effects of these diverse printing parameters on ceramics may differ from those observed in traditional materials commonly used in AM (Huang et al., 2021).

## **1.2 Importance of the Study**

The rheological behavior of the feedstock plays a crucial role in ensuring smooth extrusion through the 3D printer's extruder head. Additionally, it is important to determine the feedstock's thermal properties to ensure the appropriate temperature for printing and thermal debinding. The mechanical properties of the sintered sample are also vital in assessing the quality of the final ceramic-based AM product. This research aims to investigate the impact of varying the ceramic loading and chemical solvent in the solvent debinding process on the feedstock's thermal properties, rheology behaviour, physical and mechanical properties of the resulting ceramic-based AM product, specifically using Zirconia in FDM. By conducting series of testing and analysing, ceramic-based AM able to optimize its mechanical characteristics. Moreover, it is crucial to investigate the microstructure of the sintered specimen, which may vary during the high-temperature sintering process. Overall, this research serves as a springboard for future development in ceramic-based AM, enabling the optimization of its mechanical characteristics.

### 1.3 Problem Statement

There were many studies on the feasible thermoplastic binder for ceramic-based AM, the rheological properties of the feedstock, debinding method and sintering processes of the green sample, and the impact of different printing parameter on mechanical properties.

However, limited research has focused on exploring the rheological and thermal properties of the feedstock containing Zirconia with different solid loading. Besides, there is a lack of research into the mechanical properties of sintered samples with different chemical solvent debinding and ceramic solid loading. In addition, a question remains uncertain how much the mechanical properties will be affected by altering a single printing parameter using the FDM method.

Therefore, it is desirable to conduct a comprehensive study examining the rheological and thermal properties of the feedstock with varying the solid loading. Mechanical testing should be performed on sintered samples subjected to different chemical solvents in the debinding process, ceramic solid loading and determining printing parameter that optimize the mechanical properties.

### 1.4 Aim and Objectives

The primary goal of this project is to propose the best, chemical solvent, ceramic solid loading and printing parameters based on the mechanical properties of ceramic-based AM using the FDM method with Zirconia as the ceramic material. Success in this research would increase the likelihood of ceramic-based AM becoming the dominant fabrication method for fully functioning mechanical components. The following are the specific objectives of this study to accomplish this:

- (i) To evaluate rheology behaviours and thermal properties of feedstock.
- (ii) To evaluate the physical and mechanical properties of sintered structural part with different ceramic solid loading, printing parameters and chemical solvent.
- (iii) To determine the best chemical solvent for solvent debind.
- (v) To study the morphology of sintered structural part.

### **1.5 Scope and Limitation of the Study**

This research project will utilize various laboratory equipments such as a Brabender plastograph, a 3D printer, and a furnace for preparing ceramic-based (Zirconia) AM feedstock and specimens. Rheology studies and mechanical testing were conducted using analytical equipment such as a rheometer, a universal testing machine, and a hardness testing machine, along with relevant analytic software. Furthermore, the best solid loading, debinding solvent and printing parameters were determined based on the mechanical properties. The microstructure of the sintered specimens were studied using scanning electron microscopy (SEM) and X-ray diffraction (XRD).

However, it is important to note that this research will not cover the study of the sintering process. Additionally, physical properties such as surface roughness and porosity, which may be influenced by solid loading and debinding solvent, will not be examined.

## CHAPTER 2

### LITERATURE REVIEW

#### 2.1 Introduction

Additive manufacturing (AM), or 3D printing, has become a major topic due to its potential for sustainable production. This technology allows for the creation of customized products without the need for manufacturing molds or tools, and with minimal material waste. Several AM techniques have been developed, including Fused Deposition Modeling (FDM), Stereolithography, Material Extrusion, Power Jetting, and Binder Jetting. FDM stands out among these techniques due to its efficacy in prototype printing (Shaik, Schuster and Shaik, 2021). However, FDM is still an immature method for ceramic-based AM using Zirconia. Ceramic-based AM using Zirconia has the potential to play a critical role in various fields, such as manufacturing, biomedicine, and aerospace. Several types of literature reviews are conducted to learn more about:

- (i) Ceramic Based Additive Manufacturing Overview
- (ii) Thermogravimetric analysis
- (ii) Rheological Properties and Mechanical Testing
- (iii) Printing Parameter
- (iv) Type of Solvent in Solvent Debinding
- (v) Scanning Electron Microscope
- (vi) X-ray Diffraction Analysis

#### 2.2 Ceramic-Based Additive Manufacturing Overview

Additive manufacturing (AM) is a technique that constructs small and complex components layer by layer to create a three-dimensional object controlled by a 3D printer using commands generated by slicing software (Solomon, Sevel and Gunasekaran, 2021). This technology offers benefits such as design flexibility, minimal material waste, fewer production processes, and cost-effectiveness (Shaik, Schuster and Shaik, 2021), making it ideal for low-volume manufacturing and customised components that do not require costly mold tooling, typically used for high-volume production. However, there are several drawbacks to employing AM, such as limited material availability, limited

building size, and lengthy post-processing time (Solomon, Sevel and Gunasekaran, 2021). Since AM is not typically used for large-size manufacturing, the product must be designed into smaller subparts, increasing complexity and assembly time. Additionally, lengthy post-processing times, such as the necessary debinding and sintering process, which may take dozens of hours to remove the thermoplastic binder in the 3D printed sample, are significant issues in ceramic-based AM (Huang, et al., 2021).

Among FDM, Stereolithography, Material Extrusion, Power Jetting, Binder Jetting, etc. technologies, FDM has the advantages of low equipment cost, easy operation, relatively low raw material cost, and high printing speed (He, et al., 2021). The feeder, extruder nozzle, and printing bed are the three most critical components in FDM 3D printing. The feeder's function is to feed or provide a location for the feedstock, depending on the type of feedstock. The two most frequent types of feedstocks are filament and pellet. The key difference between these two feedstocks is that filament feedstock is generally more expensive than pellet feedstock due to the manufacturing process and the recyclability of pellet feedstock, which can be fed to the extruder again. However, filament feedstock usually provides better printing quality and surface finish than pellet feedstock due to porosity, under extrusion, or over extrusion. There are two types of extruders for filament and pellet feedstocks: filament extruders and pellet extruders. Both types of extruders operate on the same concept: heat the material to the glass transition phase and extrude it onto the printing bed through the nozzle. The fundamental difference between these two extruders is that filament extruders transport feedstock from the inlet to the nozzle using a simple driving motor, while pellet extruders transfer feedstock from the intake to the nozzle using an Auger screw (Shaik, Schuster, and Shaik, 2021). Additionally, the printing bed may be regulated to a specific temperature to ensure that the hot printed feedstock does not shrink when in contact with the plate, which can result in poor printing quality and inability to adhere to the plate.

Figure 2.1 shows the five phases in multi-step ceramic-based AM: synthesis of ceramic material and binders, the printing of material, solvent debinding, thermal debinding, and sintering. Due to the brittle nature of ceramic materials, even with a 30 % solid loading, pellet feedstock is often utilised in

multi-step ceramic-based AM employing FDM such as Alumina, Zirconia, Silicon Nitride, and carborundum (He, et al., 2021). Furthermore, ceramic material has an exceptionally high melting temperature and little ductility, making it exceedingly difficult to extrude it through the nozzle of the extruder head. Furthermore, the thermal shock resistance of ceramic material is low, resulting in cracking and porosity during 3D printing. To overcome the obstacle and meet the FDM requirement, thermoplastic binders are synthesised with the ceramic material in the feedstock preparation (Lakhdar, et al., 2021). The thermoplastic binders may perform the functions of a plasticiser, backbone binder, and additives. The plasticiser is the primary binder in the feedstock that reduces viscosity and increases ductility. The backbone binder provides a cohesive force between the particles to preserve structural integrity. At the same time, the additive acts as a surfactant in the feedstock to guarantee the feedstock may extrude smoothly and uniformly through the nozzle of the extruder head without clogging (Huang, et al., 2021). According to Huang, et al. (2021), the binder-coated zirconia feedstock had 87.0 wt% zirconia and 13 wt% binders. Polyethylene (PE) copolymer included 6.5 wt% acted as the backbone binder, paraffin wax (PW) contained 5.2 wt% acted as the plasticiser, and stearic acid (SA) contained 1.3 wt% served as the surfactant for material extrusion feedstock in the 13 wt% of binders. Furthermore, He et al. (2021) reported that 85 wt% of ceramic solid loading was combined with 15 wt% of binders during the synthesized of feedstock for FDM employing screw extrusion. The binders contained 7.5 wt% PW, 3.75 wt% ethylene-vinyl acetate copolymer, 3 wt% PE, and 0.75 wt% SA to reduce viscosity, enhance adhesive and cohesive force, and function as a composite surfactant.

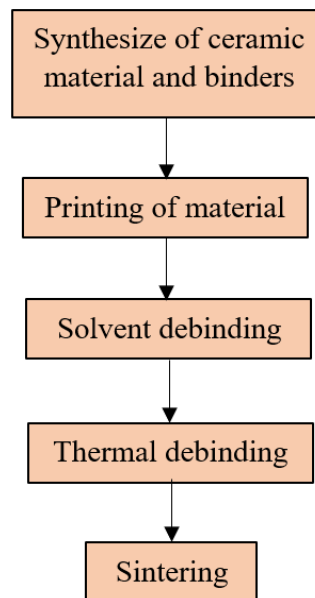


Figure 2.1: Processes of Multi-step AM

Following feedstock preparation, the ceramic green body may be printed layer by layer using the software's command. A 3D computer-aided design (CAD) model is built and saved as a Standard Triangle Language/Standard Tessellation Language (STL) file. The 3D model will next be sliced by slicing software for generate the G-code for printing, which refers to the printing parameter. Finally, the G-code will serve as the printing process's instruction.

Finally, the printed green body will undergo debinding and sintering to produce a dense and robust debound sample by removing the thermoplastic binders (Lakhdarm, et al., 2021). In general, there are two processes in the debinding process: solvent debinding and thermal debinding. Solvent debinding removes most of the binder from a green body by immersing it in a chemical solvent and keeping it at a constant temperature. Thermal debinding removes the leftover binder by gradually raising the temperature of the solvent-debound substance. The temperature gradually rises to avoid breaking, owing to the ceramic material's limited thermal shock resilience. The debound body is sintered at a very high temperature in a furnace (He, et al., 2021). This was shown by Huang, et al. (2021), who used heptane in a water tank at 35 °C for a day before drying at room temperature for 4 hours to remove more than 99 % of PA and SA binders. The solvent debound body was then heated for forty-

three hours at varying heating rates in a stepwise fashion in the thermal debinding procedure to eliminate the residual binders. Finally, the debound body was sintered using varied heating rates in a stepwise method to achieve the desired temperature of 1350 °C, which was maintained for one to three hours. The thermogravimetric analysis (TGA) is used to determine the heating rate of the thermal debinding and sintering process. The dense and robust ceramic-based printed part is ready for use after the debinding and sintering processes.

### **2.3 Thermogravimetric Analysis**

TGA is an analytical method that uses weight change to assess both the thermal stability of a material and the quantity of volatile components it contains. This method is essential in multi-step ceramic-based AM, as the temperature required to remove the binder during the thermal debinding process greatly influences the success of the subsequent sintering process, which occurs at a considerably higher temperature (Nötzel, Eickhoff, and Hanemann, 2018).

Huang, et al. (2021) conducted TGA to investigate the thermal properties of the feedstock. The analytical results showed that the feedstock binder began to degrade at 137 °C, leading to a reduction in weightage. The binders were entirely removed at 515 °C, resulting in a consistent weightage equivalent to that of the ceramic-based material. In addition, the gradient of the TGA result determines the heating rate for thermal debinding, with a higher gradient indicating that more binder is degraded simultaneously as the weightage decreases. As a result, stepwise temperature control may be employed during the thermal debinding process to minimize cracking caused by a rapid reduction in the binder. Moreover, Nötzel, Eickhoff, and Hanemann (2018) noted that the thermal debinding process may be halted at a low gradient temperature before the binder is entirely removed. This is because mechanical stability must be ensured when transporting the thermally debound sample to the sintering furnace, even if some binder remains, as the sample will become brittle if all binders are removed.

### **2.4 Rheological Properties and Mechanical Testing**

The study of rheology is essential in FDM technology because the flow and deformation of the feedstock play a crucial role in determining the quality of the



resulting AM part. A well-deposited feedstock reduces porosity and cracking during the debinding and sintering processes, resulting in a high-quality debound product (Lakhdar, et al., 2021). To evaluate the rheological behaviour of the feedstock, a rheometer was used. The viscosity of the feedstock must be low enough to allow smooth extrusion without nozzle clogging while retaining the desired shape after extrusion and when subjected to successive layers of deposition material (Arrigo and Frache, 2022). The ratio and weightage of the thermoplastic binders and ceramic material are critical factors that affect the rheological behaviour of the feedstock (Prabhu and Devaraju, 2020).

Apart from that, mechanical testing of sintered samples is crucial for studying their mechanical performance as the mechanical properties of ceramic-based AM can affect its range of applications and safety factor. By predicting the behaviour of the material, mechanical testing helps engineers select the appropriate material during the design phase. Various mechanical tests, such as tensile testing, three-point bend testing, compressive testing, and hardness testing, must be performed on specimens with dimensions defined by international standard organizations like the International Organization for Standardization (ISO) and the American Society for Testing and Materials (ASTM), using the appropriate testing machine, loading cell, and grip fixture. As a result, mechanical testing can be employed to evaluate the factors that influence the mechanical properties of ceramic-based AM produced using FDM.

#### **2.4.1 Viscosity and Linear Viscoelastic Range**

When measuring the rheological properties of feedstock viscosity by adjusting the shear rate, the feedstock can be classified as a Newtonian or non-Newtonian fluid. Figure 2.2 shows that Newtonian fluids exhibit constant viscosity as the shear rate increases. Non-Newtonian fluids, however, exhibit shear thickening (dilatant) or shear thinning (pseudoplastic) behaviour. As the shear rate increase, the viscosity may increase or decrease, depending on whether it is thickening or thinning, respectively (RheoSence, 2022).

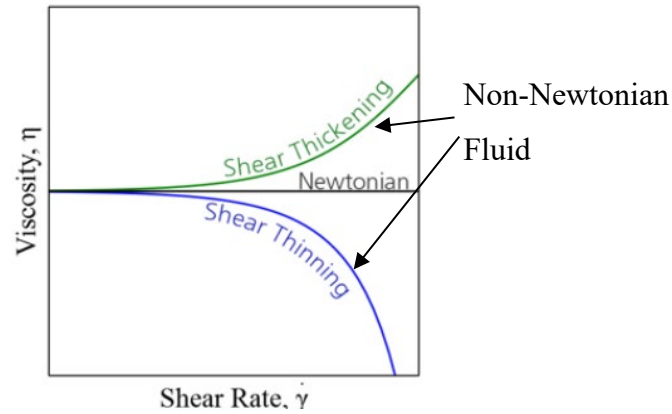


Figure 2.2: Viscosity Behaviour of Newtonian and non-Newtonian Fluid (RheoSence, 2022)

According to Huang et al. (2021) and Masuda, Ohta, and Kitayama (2019), the feedstock used in FDM technology should exhibit shear-thinning behaviour. This allowed the feedstock to be extruded through the nozzle with minimal extrusion force, as the viscosity gradually decreases when subjected to small increases in shear rate. For instance, the ceramic-based feedstock of piston-based material extrusion, made up of zirconia and polymer binders, demonstrated shear-thinning properties, enabling smooth extrusion with a low piston extrusion force (Huang, et al., 2021). Similarly, Masuda, Ohta, and Kitayama (2019) demonstrated that the silicon carbide ceramic-based feedstock used for powder and slurry-based 3D printing also exhibited shear-thinning properties.

Furthermore, Huang, et al. (2021) conducted an oscillatory temperature sweep test and discovered that the viscosity of zirconia ceramic-based feedstock with polymer binders increased as the temperature raised. The oscillation strain used in the test must fall within the linear viscoelastic range, which is defined at a constant value of 0.03 %. The oscillatory strain sweep was used to determine the linear viscoelastic range, and by adjusting the oscillatory strain, the storage modulus ( $G'$ ) and loss modulus ( $G''$ ) can be observed in this oscillatory strain sweep. According to Figure 2.3,  $G'$  and  $G''$  will remain constant at low oscillatory strain, indicating the linear viscoelastic range, and will begin to decline once the oscillatory strain exceeds the critical oscillatory strain.

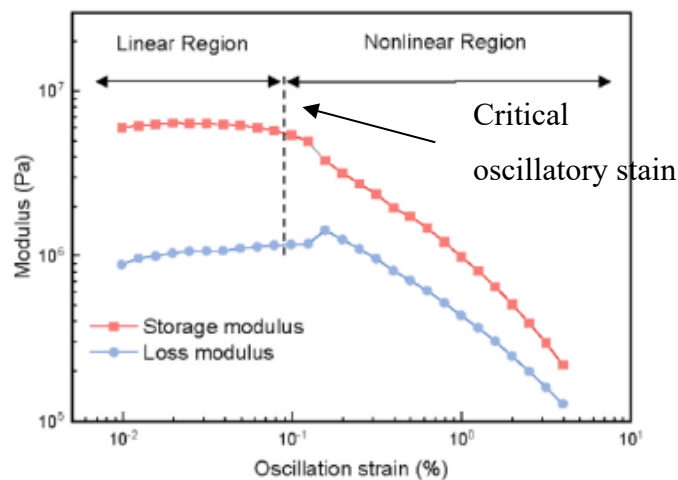


Figure 2.3: Result of Oscillatory Strain Sweep (Huang, et al. 2021)

Additionally, the researchers showed that initially,  $G'$  is greater than  $G''$  and gradually decreases to where  $G'$  becomes less than  $G''$  as the oscillatory strain increases. This indicates that the feedstock had solid-like properties that change to liquid-like properties, enabled the feedstock to extrude through the extruder head at the correct temperature. The crossing points of the  $G'$  and  $G''$  were referred to as the shear yield strain, as illustrated in Figure 2.4 (Huang, et al., 2021).

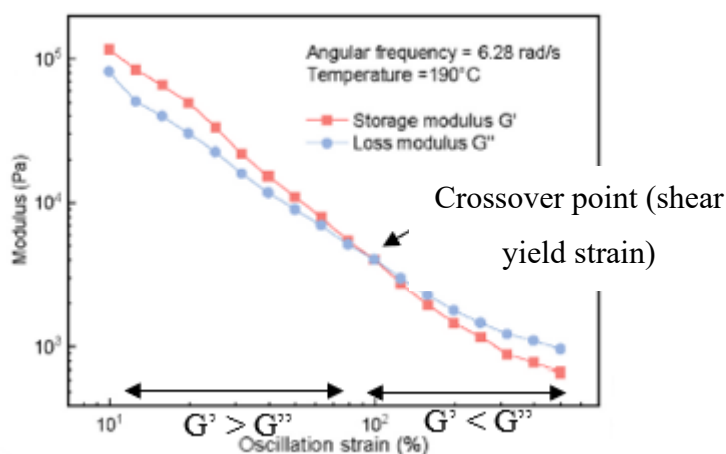


Figure 2.4: Shear Yield Strain (Huang, et al. 2021)

Furthermore, the concentration of binder or solid loading significantly impacts the viscosity of ceramic-based feedstock. Previous research (Zhang et al., 2019) demonstrated this by using Alumina ceramic-based slurry for

stereolithography with KOS110 as the dispersant, which functioned similarly to a binder in decreasing viscosity. The findings showed that increasing the concentration of dispersant lowered the viscosity of the slurry. However, once the concentration of dispersant exceeded the saturation threshold, the viscosity of the slurry begins to increase due to bridging flocculation, which occurs when an Alumina particle adsorbs more than one KOS110 particle. Moreover, the study found that increasing the solid loading progressively modifies the viscosity of the Alumina slurry. When the solid loading was increased, the viscosity of the Alumina slurry with a constant concentration of dispersant also increased. The rheological behaviour remains entirely Newtonian when the solid loading was less than or equal to 60 %. However, as the solid loading increased, the viscosity first raised and then fall as the shear rate increased. This irregular behaviour of the feedstock rheology is unsuitable for AM because it lowers the quality of printed items due to material structure inconsistencies. Therefore, it is essential to use the appropriate binder concentration and solid loading, which will progressively influence the viscosity of the ceramic-based feedstock for AM.

#### **2.4.2 Tensile Test**

During a tensile test, a testing sample is elongated by holding both ends of the sample until it reaches its breaking point, and the elongation of the sample and the tension force applied are recorded. Tensile samples are often shaped like a dog bone, as shown in Figure 2.5 below. The various mechanical characteristics of the material, such as tensile modulus, ultimate tensile strength, and yield strength, can be determined by plotting a stress-strain graph (Saba, Jawaid, and Sultan, 2018). Tensile modulus, also known as the modulus of elasticity, is the ratio of tensile stress to strain under elastic deformation. It refers to the tension force that can be applied to the specimen and how much it can stretch before returning to its original length when the force is removed. Besides, yield strength is the stress applied that causes the specimen to undergo plastic deformation, which it will not return to its original length. Finally, the ultimate tensile strength is the highest stress the specimen can withstand before it breaks. Thus, tensile testing can inform engineers about how strong a material is and how far it can be stretched before breaking.

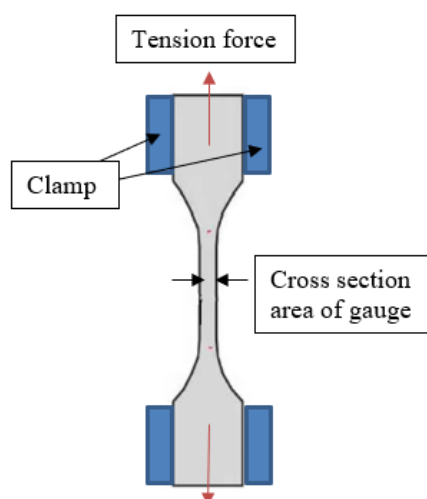


Figure 2.5: Dog Bone Shape Sample for Tensile Test

Furthermore, ASTM has established several other standards with varying dimensions. For example, Huang, et al. (2021) conducted tensile tests to determine the ultimate tensile strength of the specimen using the ASTM C1273 testing standard for zirconia. However, the researcher reduced the sample size to avoid errors caused by bending formation during the sintering process. Furthermore, Liu, Lei, and Xing (2019) conducted a tensile test by fabricating a dog bone shape sample with the dimensions specified in ASTM D638, a testing standard applicable to reinforced or non-reinforced plastic. Researchers discovered that printing parameters such as build orientation, raster angle, and layer height significantly impacted the final tensile strength (Liu, Lei and Xing, 2019; Huang, et al., 2021). Furthermore, while doing tensile tests, selecting an appropriate standard is critical since using the incorrect standard might affect the accuracy of the results.

### 2.4.3 Flexural Test

The flexural test is a method used to determine the stiffness of a material by measuring the force required to bend a bar-shaped sample. The resulting stress-strain graph can reveal mechanical characteristics like flexural modulus and ultimate flexural strength. Flexural modulus, which measures a material's ability to bend, is defined as the ratio of flexural stress to strain. A higher flexural modulus value indicates that the material is stiffer, while a lower value indicates

that the material is more flexible and bendable. Ultimate flexural strength, on the other hand, is the maximum bending force that a material can withstand before it fractures.

The most common test used to determine flexural properties is the three-point bending test. This test measures the force required to bend a bar-shaped sample under three-point loading conditions, where the sample is placed on two support pins with a support span at both ends, and force is applied at the centre, as shown in Figure 2.6. The support span, sample thickness, rate of load increase, and maximum deflection in a three-point bend test are all described differently by ASTM and ISO standards. For example, ASTM D790 specifies a maximum deflection of the sample to stop testing at 5 %, while ISO 178 specifies that the test continues until the sample breaks (Saba, Jawaid, and Sultan, 2018). Moreover, ASTM C1161 is a suitable testing standard for ceramic materials that performs flexural tests using cylindrical rollers for support and load until the sample breaks to record the breaking force (Huang et al., 2021). Liu, Lei, and Xing (2019) found that build orientation, raster angle, and layer height significantly affected the ultimate flexural strength of the AM specimen.

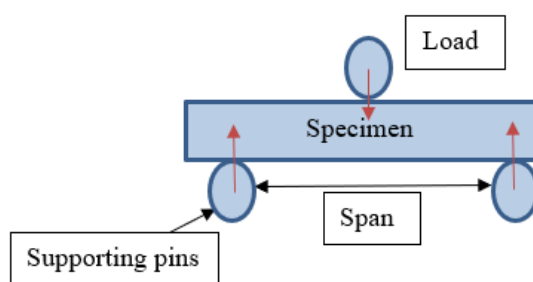


Figure 2.6: Three-point Bending Test

#### 2.4.4 Compressive Test

The compressive test is performed by applying a constant displacement rate compressive force to the sample to determine the material's compressive strength that can bear without fracture. During the test, the sample's deformation under compressive force is recorded until it fractures, and a stress-strain curve is generated. Buckling must be avoided during the compressive test to obtain an

accurate result, which necessitates the use of compression fixtures with precise alignment and guiding. To avoid buckling, the length-to-diameter ratio of 2:1 is used. Additionally, "compression after impact" is a type of compression test in which the specimen is subjected to an impact force before the compressive test to demonstrate advancements in damage-tolerant composites and composite performance repeatability (Saba, Jawaid and Sultan, 2018). Furthermore, compressive tests can determine compressive modulus, which is the ratio of compressive stress to strain.

Huang, et al. (2021) investigated the compressive strength of zirconia ceramic-based AM using cylindrical samples with ASTM C1424 dimensions. Their study revealed that AM zirconia ceramic performs well in compressive tests due to the ability of fractures and defects to close when crushed, thereby preventing the development of new cracks. Furthermore, the study found that the raster angle of the FDM sample did not affect the output due to the cylindrical shape of the sample. However, the layer thickness of the printed item had a significant impact on compressive strength, as thinner layers led to a larger adhesive force between each printed layer and reduced the number of voids in the printed sample.

#### **2.4.5 Hardness Test**

There are various methods for hardness testing, including the Vickers hardness test, Brinell hardness test and Rockwell hardness test. The goal of all these methods is to investigate a material's resistance to permanent indentation or scratching by pressing a specified dimensioned indenter into the surface of the sample. The choice of testing method depends on the available equipment and type of material, and each method has its own standards for each material. For example, the ASTM E10 standard is used for metallic Brinell hardness testing with a ball indenter. The hardness value is calculated by measuring the circular indentation left by the applied force. The ASTM E18 standard is used for the Rockwell hardness test, which uses a ball or diamond indenter. During the test, a preliminary load is applied for a brief period, and the indentation is measured and recorded. Then, a higher force known as the main load is applied, followed by reapplying the preliminary load, and the final indentation is measured and recorded. The Rockwell hardness is determined by subtracting the preliminary

and final indentation values. For Vickers hardness testing, which has the ASTM C1327 standard for ceramics, a diamond indenter is used with a force of 1 kg for 10 seconds, and the indentation is measured to compute the Vickers hardness of the material. Huang, et al. (2021) demonstrated that varying the printing parameters of an AM printed object has no significant influence on hardness.

## **2.5 Printing Parameter**

Various printing factors influence the printing quality, mechanical and physical properties of a printed object. The printing parameters can be divided into two groups: machine parameters, such as extrusion temperature and nozzle diameter, and working parameters, such as build orientation, layer thickness or height, air gap, raster angle, infill pattern and density, extrusion temperature, and raster width (Kristiawan, et al., 2021). Machine parameters are determined by the settings or parts used in the 3D printer, while working parameters are determined by the slicing software input. Therefore, to optimize the printing parameters of ceramic-based AM, a thorough study of these printing parameters is required.

### **2.5.1 Build Orientation**

In terms of build orientation, the FDM can be carried out using flat (X-direction), on-edge (Y-direction) or upright (Z-direction) orientation, as shown in Figure 2.7 below. According to Liu, Lei, and Xing (2019), upright orientation was unsuitable for FDM since most PLA composite parts, such as ceramic, copper, and aluminium-based, do not print entirely. Furthermore, as the construction orientation changed from 0° (flat) to 90° (on-edge/upright), the final compressive strength of the printed item decreases, as did the tensile strength, with a maximum loss of 60%. (Solomon, Sevel and Gunasekaran, 2020). However, Liu, Lei, and Xing (2019) demonstrated that on-edge construction orientation provided higher value in terms of flexural and tensile strength. As a result, it is critical to research the impact of tensile and flexural strength by changing the construction orientation.



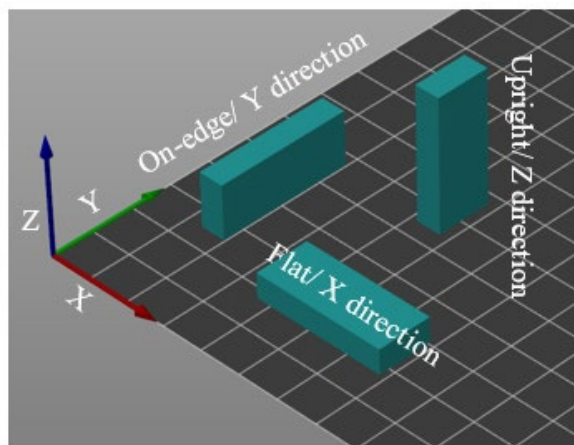


Figure 2.7: Build Orientation

### 2.5.2 Layer Height

Layer height or layer thickness is the amount of feedstock deposited on the printing bed in the Z-axis when the extruder travels along the printing route once, as illustrated in Figure 2.8 below. Additionally, the maximum layer height is always less than the nozzle's diameter (Solomon, Sevel, and Gunasekaran, 2020). In addition, Huang, et al. (2021) conducted tensile, compression, hardness, and flexural tests on specimens printed with three different layer heights of 2mm, 3mm, and 4mm. The test results revealed that the lower the layer height, the stronger the tensile, compression, and flexural strength due to enhanced bonding between the layers, resulting in a denser and less porous printed product. However, the layer height of the printed product did not affect its hardness.

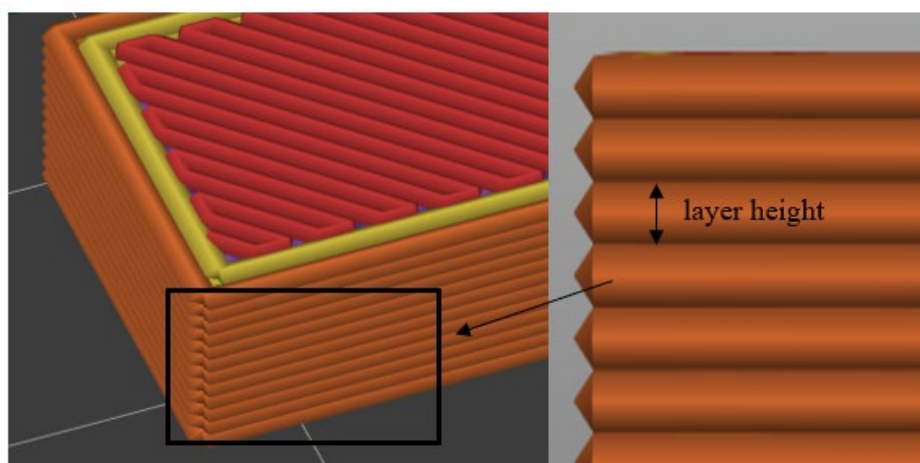


Figure 2.8: Layer Height

### 2.5.3 Raster Angle

Raster angle refers to the angle between the printing path of the 3D printer and the x-axis direction of the printing bed. Typically, multiple raster angles can be used in FDM, such as  $0^\circ/90^\circ$ ,  $30^\circ/-60^\circ$ , and  $45^\circ/-45^\circ$ , as illustrated in Figure 2.9. Each produces a different output in terms of mechanical characteristics. Solomon, Sevel, and Gunasekaran (2020) and Huang, et al. (2021) had shown that the raster angle of the printed sample had no influence on flexural strength and hardness but had a steady decrease in tensile strength as the raster angle increases from  $0^\circ$  to  $45^\circ$ . However, due to the cylindrical form of the testing sample, as specified in ASTM C1424, the compressive test was not included in the study. As raster angles are variable, identical printed samples will be produced in a symmetrical form.

On the other hand, Liu, Lei, and Xing (2019) had demonstrated that the raster angle has a considerable effect on both tensile and flexural strength. Furthermore, the researchers revealed that a raster angle of  $45^\circ/-45^\circ$  yields stronger tensile and flexural strength, which is opposite to the results obtained by Solomon, Sevel, and Gunasekaran (2020) and Huang et al. (2021). As a result, it is critical to investigate the influence of tensile and flexural strength by adjusting the raster angle.

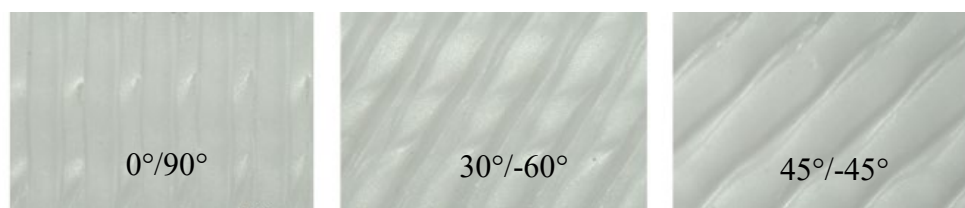


Figure 2.9: Raster Angle of Printed Sample (Huang, et al., 2021)

### 2.5.4 Air Gap

During AM, the air gap is the distance between two consecutive printed feedstock routes that may be classified as positive, zero, or negative. A positive air gap shows that the printed feedstock routes are spaced apart. A positive air gap will result in a faster printing time but a lower mechanical performance due to the loosely packed structure. A zero-air or negative air gap implies that the printed feedstock is attached side by side or overlaps with the next printed feedstock. As a result, as a denser item is printed, the zero-air gap will give

better mechanical performance than a positive air gap, and a negative air gap will provide the greatest results. A negative air gap, on the other hand, is employed only when time is not an issue in the process since it would result in a lengthier printing time (Solomon, Sevel and Gunasekaran, 2020).

### 2.5.5 Infill Density and Pattern

Infill density significantly impacts the printed product's mechanical qualities—a lower infill density results in a poor mechanical property and a low-density printed sample. In contrast, a higher infill density results in optimum mechanical characteristics and a nearly full density printed sample. However, a lower infill density printed item needed less time to print than a full density printed sample (Solomon, Sevel and Gunasekaran, 2020).

Aside from that, as illustrated in Figure 2.10, there are other infill patterns accessible in AM for the interior structure of the printed item, including linear, grid, triangles, and hexagons. Only the linear and concentric infill patterns can provide a complete infill density due to the presence of voids in the other infill patterns. Furthermore, different infill patterns may result in superior performance in certain types of mechanical tests. For example, a particular infill pattern may have high tensile strength but relatively low flexural strength.

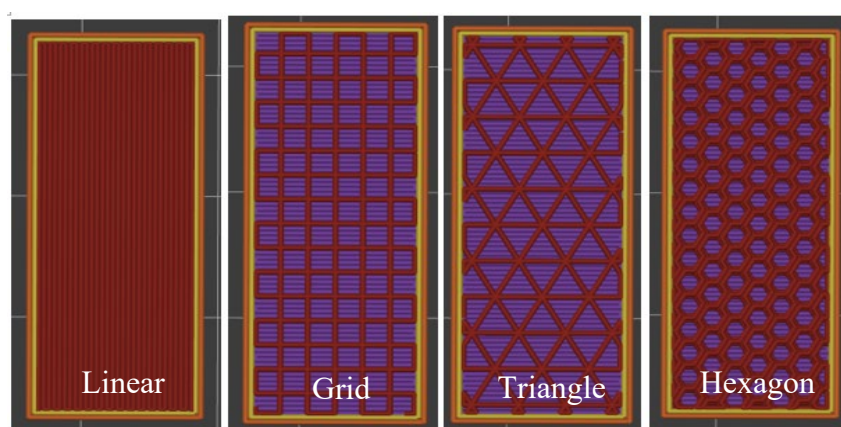


Figure 2.10: Infill Pattern

### 2.5.6 Extrusion Temperature

The temperature at the nozzle of the FDM extruder head before the feedstock is deposited on the printing bed is known as the extrusion temperature. The extrusion temperature must be maintained throughout the printing process since

it affects the viscosity of the feedstock, which can impact the volume of extruded feedstock. Additionally, the internal tension created during the temperature decrease when the feedstock is extruded and placed on the printing bed may cause deformation or printing failure (Solomon, Sevel, and Gunasekaran, 2020). Moreover, the optimal extrusion temperature may differ when the solid loading and binder ratios are different, even when using the same base material feedstock. Hence, it is crucial to determine the appropriate extrusion temperature of the feedstock as it can impact printing quality.

### 2.5.7 Nozzle Diameter and Raster Width

In terms of raster width, as illustrated in Figure 2.11, it refers to the width of the printing path that is largely influenced by the nozzle diameter. The nozzle diameter also significantly affects the printing time since a smaller diameter nozzle extrudes less material within the same time frame compared to a larger diameter nozzle. Consequently, a smaller nozzle diameter results in a narrower raster width, which leads to a longer printing time to complete the process. However, using a smaller nozzle diameter and raster width typically results in less geometrical error (Solomon, Sevel, and Gunasekaran, 2020).

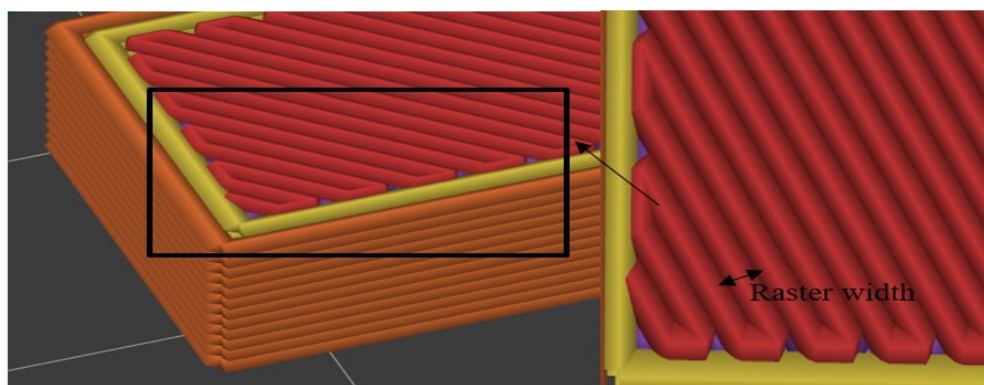


Figure 2.11: Raster Width

### 2.6 Type of Solvent in Solvent Debinding

Solvent debinding is a ceramic-based AM technique used to remove most of the binder by immersing the green body in a chemical solvent. The density and number of porosities in the solvent debound portion are affected by the chemical solvent utilized. Furthermore, the type of chemical solvent used in solvent

debinding is significant in ceramic-based AM since it affects the mechanical performance of the printed object. Therefore, Li, et al. (2020) conducted experiments to investigate the influence of density and mechanical properties using several types of chemical solvents. The study involved printing an alumina ceramic-based green body with photosensitive resins as the binder using stereolithography AM technology. The solvent debinding process used a different chemical solvent, followed by the same thermal debinding and sintering procedure to manufacture a dense alumina-based 3D printed object.

The reduced density of the solvent debound sample compared to the base material suggests that not all binders were entirely removed during the solvent debinding process. However, Li, et al. (2020) demonstrated that the density of the solvent debound sample was not the most critical factor in determining the final density of a sintered sample. This is because the temperature of the sintering process was much higher than that of the debinding process, which were 1500 °C and 550 °C, respectively. Similarly, Huang, et al. (2021) used a lower temperature in the debinding process compared to the sintering process, which were 500 °C and 1350 °C, respectively. Furthermore, heptane was used to debind the printed sample, and only 5.3 wt% of the binders were lost during the solvent debinding process, while the remaining weightage of binders was lost after the thermal debinding and sintering process.

Although the chemical debinding solvent has no direct effect on a sintered object's final density, it impacts its mechanical qualities. Li, et al. (2020) demonstrated that when various types of debinding solvents were used, the flexural strength of the sintered sample may be reduced by up to 50 %, with a maximum of 63.4 MPa and a minimum of 32.6 MPa. When oxalic acid was used as the chemical debinding solvent, the alumina ceramic-based photosensitive resin binder will provide the highest flexural strength. At the same time, utilising dimethyl carbonate as the chemical debinding solvent results in a sintered product with the lowest flexural strength, even though both had a similar bulk density and open porosity percentage after the solvent debinding process. Furthermore, while had a low bulk density and a large open porosity percentage of solvent debound sample, the chemical debinding solvents ethyl alcohol and polyethylene glycol provided a moderate performance in flexural strength. As a result, it can be concluded that the kind of chemical

solvent used in the solvent debinding process directly impacts the mechanical characteristics of a sintered sample, and more research in this area is required.

## **2.7 Scanning Electron Microscope**

SEM is an advanced microscopy technique used to generate high-magnification and high-resolution images by using a focused beam of high-energy electrons. Through SEM, the morphology, chemical composition, and crystalline structure of solid specimens at micro- and nanoscale can be determined (Swapp, 2017). Researchers had utilized SEM to study the morphology of sintered zirconia specimens by observing the grain size and porosity. The surface of the samples was polished, followed by a process called thermal etching at a temperature of 1000 °C for one hour. The purpose of polishing is to ensure that the surface is flat, smooth, and free of micro-scratches, while thermal etching enhances the visibility of grain boundaries. Lastly, the samples were coated with a conductive material such as platinum to preserve the original surface morphology, providing a conductive surface for the electron beam to interact with and reduce charging effects, thereby improving the resolution of the image capture (Huang, et al., 2021). However, there is insufficient research to prove the effect of solid loading on the grain size of sintered zirconia samples. Therefore, it is essential to conduct further investigations to determine whether there are any changes in grain size when the solid loading is varied.

## **2.8 X-ray Diffraction analysis**

XRD is a powerful analytical technique that is commonly used to study the crystal structure of a material. XRD uses monochromatic X-rays directed at a crystalline sample to produce constructive interference and a diffracted ray, a peak in intensity occurs when conditions satisfy the Bragg's Law ( $n\lambda=2d \sin \theta$ ). The diffracted X-rays are then detected and counted to identify the mineral based on its unique d-spacings. X-rays generated in an X-ray tube and directed at the sample, with the angle between the incident and diffracted rays being a key component of all diffraction during XRD (Dutrow and Clark, 2023). With the peak intensity at the  $2\theta$  angle, the crystallographic shape with miller indices present in the specimen can be determined.

In addition, Neacsu, et al. (2016) stated that pure zirconia had a total of three different crystallographic shapes, each of which was stable at different temperatures: monoclinic, tetragonal, and cubic, as shown in Figure 2.12. However, the crystal structure of zirconia may undergo spontaneous phase transformation from tetragonal to monoclinic when cooled. The phase transformation causes changes in volume and structural defects that affect the material's mechanical properties. Therefore, doping agents such as yttria are used to stabilize the structure, and the concentration of the doping agent used affects the phase diagram, as shown in Figure 2.12. Therefore, it is important to perform XRD on the sintered zirconia 3D-printed specimen as it has undergone a high-temperature sintering process.

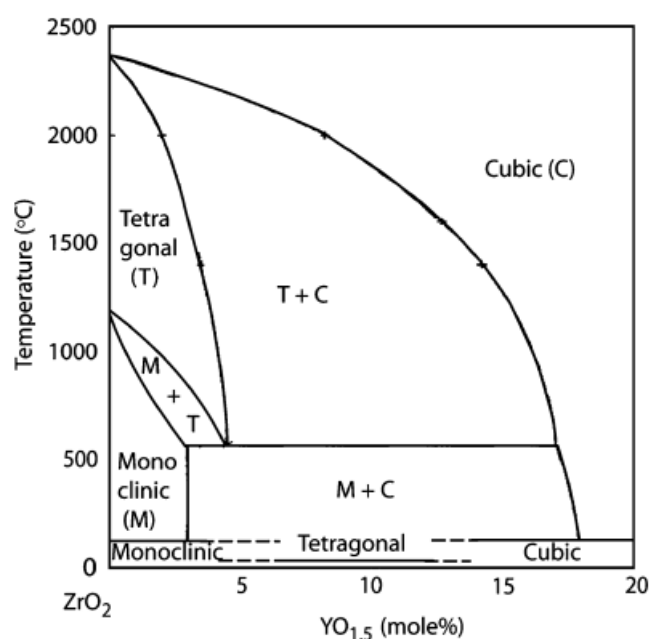


Figure 2.12: Phase diagram of yttria-stabilized zirconia (Witz et al., 2007)

## 2.9 Summary of Literature Review

In summary, AM technology creates a three-dimensional object layer by layer, controlled by a 3D printer. AM is cost-effective and ideal for low-volume manufacturing and customized components but has drawbacks such as limited material availability, limited building size, and lengthy post-processing time. Fused deposition modelling (FDM) is a commonly used AM technology, and its components include the feeder, extruder nozzle, and printing bed. Multi-step ceramic-based AM using FDM is challenging due to the brittle nature and high melting temperature of ceramic materials. To overcome these challenges,

thermoplastic binders such as PW, SA, and LDPE were used in the feedstock preparation phase. The ceramic green body is printed layer by layer using a 3D CAD model saved as a STL file and sliced into G code. The five phases in multi-step ceramic-based AM are the synthesis of ceramic material and binders, printing of material, solvent debinding, thermal debinding, and sintering.

The thermal and rheological properties of the feedstock are important factors that must be determined to ensure the sample can be printed with appropriate parameters. Besides, the thermal properties of the feedstock also help to determine the temperature and heating rate for the thermal debinding. Mechanical tests such as tensile tests, flexural tests, compressive tests, and hardness tests were used to determine the quality of the sintered zirconia 3D printed specimen. As stated by recent researchers, the mechanical properties will be much affected by the printing parameter. However, there were different outcomes between them. Solomon, Sevel, and Gunasekaran (2020) found that compressive strength and tensile strength decreased when the orientation changed from flat to on-edge but Liu, Lei, and Xing (2019) demonstrated that on-edge provided a higher value. Besides, Solomon, Sevel, and Gunasekaran (2020) and Huang, et al. (2021) shown that there was no influence on flexural strength but tensile strength decreases when the orientation changed from 0° to 45°, but Liu, Lei, and Xing (2019) demonstrated that a raster angle of 45° provided the highest flexural and tensile strength. Aside from printing parameters, there is a lack of research on the effect of solid loading on the mechanical properties. Thus, it is crucial to find out which printing parameters and solid loading provide the highest mechanical properties for sintered zirconia specimens. In addition, researchers had found out that the type of chemical solvent used in solvent debinding had no significant effect on the final density of sintered samples but had an influence on the mechanical properties of sintered samples.

Lastly, SEM and XRD microstructure and crystal structure of the specimen, respectively. However, there is a lack of research on how the solid loading and debinding solvent affect the morphology and microstructure of sintered zirconia 3D printed samples. Thus, it is important to carry out investigations in this field.



## CHAPTER 3

### METHODOLOGY AND WORK PLAN

#### 3.1 Introduction

Ceramic-based AM technology has the potential for innovation in the fabrication of products with complex structures and geometries that are difficult or impossible to create using traditional manufacturing processes. As a result, many industries and institutions have invested significant resources into developing ceramic-based AM using various types of ceramic materials, binders, debinding, and sintering processes, as well as analysing the rheological, thermal, mechanical, and physical properties of the feedstocks, printed and sintered samples. Ceramic solid loading of feedstock will impact the printed sample quality because they alter the rheological properties. The feedstock's viscosity should be shear thinning and low to guarantee that it can be extruded smoothly through the nozzle. Thus, the rheological behaviour of feedstock with varying solid loading needs to be investigated to ensure the desired quality of the printed sample.

Aside from solid loading and the chemical solvent used in the solvent debinding process, printing parameters significantly impact the sintered object's mechanical properties. To obtain optimum mechanical performance, various mechanical tests in different aspects, such as flexural strength, tensile strength, compressive strength, and hardness, had been carried out using sintered samples with varying solid loading, chemical solvent, and printing parameters. Furthermore, the density and weight loss of each testing sample was evaluated to ensure that the density of the sintered samples were comparable to the raw ceramic material and that the binders has been fully removed. Additionally, appropriate sample shapes and sizes for mechanical testing were selected by referring to ISO and ASTM standards.

#### 3.2 Feedstock Preparation

The feedstock used in this study was made with zirconia doped with 3 mol% of yttria, Y<sub>2</sub>O<sub>3</sub> (KZ-3YF type C), as the ceramic material, along with binders including low-density polyethylene (LDPE), PW, and stearic acid (SA). The

backbone binder, LDPE, provided a cohesive force between the zirconia particles to ensure structural integrity. PW acted as a plasticiser, reduced viscosity, and increased ductility in the feedstock. SA acted as a surfactant, ensured smooth extrusion of the material. The zirconia powder used in this research had a particle diameter of around 200 nm, a specific surface area of 9 m<sup>2</sup>/g, and a density of 6.07 g/cm<sup>3</sup>, as shown in Appendix A. LDPE had a melting temperature of 110 °C and a density of 0.923 g/cm<sup>3</sup>, PW had a melting point of 52 °C and a density of 0.93 g/cm<sup>3</sup>, and SA had a melting point of 70 °C and a density of 0.941 g/cm<sup>3</sup>.

This research was done by preparing three different types of feedstocks with varying solid loading and binders' ratio. The feedstocks were composed of 60 vol%, 65 vol%, and 68 vol% ceramic solid loadings with a 40:60 LDPE to PW binder ratio. They were utilized to investigate the rheology of the feedstocks when the ceramic solid loading was varied. Additionally, the mechanical characteristics of the various solid loadings were also investigated.

A Brabender Plastograph was used to prepare the feedstock for the composite of ceramic material and binders. The temperature of the Brabender Plastograph was adjusted to 130 °C during composite synthesis, and the mixing torque was measured during 30 minutes of mixing. Since the maximum amount that can be poured into the equipment is 50 ml, 40 ml of feedstock was produced in one batch. Thus, the composite density, weightage, and mass of each element required for 40 ml were calculated using Equations 3.1, 3.2, and 3.3. SA, which served as a surfactant, was applied at a constant rate of 2.75 mg/m<sup>2</sup> of the total surface area of the zirconia. Finally, the feedstock was crushed in a pelletiser for 3D printing.

$$m = \rho V \quad (3.1)$$

$$wt\% = \frac{m_a}{m_{total}} \quad (3.2)$$

$$\rho_{composite} = \frac{m_{total}}{V} \quad (3.3)$$

where

$m$  = mass, g

$\rho$  = density, g/cm<sup>3</sup>

$V$  = volume, cm<sup>3</sup>

wt% = weightage

*a* = type of element

### **3.3 TGA**

Following the preparation of the feedstock, TGA was performed using the Thermogravimetric Analyzer (SDT Q600) from TA Instruments to determine the feedstock's thermal stability and the percentage of volatile components by weight. The analyser utilizes independent dual balance technology and a matched pair of transducers to provide differential weight loss measurements as the temperature rises. This allowed for the determination of the percentage of thermal debinding temperature and binders degradation. The feedstock filled approximately 60 % to 75 % of the pan in the analyser. The feedstock was analysed by raising the temperature from 0 °C to 600 °C at a rate of 10 °C/min under a nitrogen atmosphere. Weight, derivative weight, and heat flow versus temperature graphs were plotted throughout the analysis.

### **3.4 Rheology Testing**

Anton Paar Rheometers (Physica MCR301) and Anton Paar Rheocompass software were used to evaluate the rheological characteristics of the feedstock in terms of viscosity and linear viscoelastic range. As the sample and temperature of the bottom plate were fixed, the feedstock was loaded on the centre of the rheometer's bottom plate. When the temperature reached the desired level, a 25.0 mm stainless steel parallel plate with a 1.0 mm gap between the parallel plates was used. Furthermore, it is important to add an appropriate amount of feedstock to avoid overfilling or underfilling, which can lead to inaccurate results. The extra sample was trimmed to get the necessary load, and the rheology test was ready to run. This research will include three rheology tests: viscosity, oscillatory strain sweeps, and oscillatory frequency sweeps.

#### **3.4.1 Viscosity**

The viscosity test was performed by adjusting the shear rate and evaluating the sample's viscosity at a constant temperature. Moreover, several temperatures, including 100 °C, 110 °C, 120 °C, 130 °C, and 140 °C, were examined to investigate the effect of temperature on the viscosity of the feedstock. The shear

rate was varied from 0.01 1/s to 100 1/s using a logarithmic ramp, and the sample viscosity was measured every 2 s for a total of 200 s. Subsequently, based on the results, a viscosity versus shear rate graph was produced.

### **3.4.2 Oscillatory Strain Sweep**

The oscillatory strain sweep test was conducted by adjusting the shear strain and measuring  $G'$  and  $G''$  at a constant temperature and constant angular frequency of 6.28 rad/s, where the optimal temperature was determined in Section 3.4.1. The linear viscoelastic range and critical oscillatory strain point of the sample were determined by varying the shear strain from 0.01 % to 100 % using a logarithmic ramp and recording  $G'$  and  $G''$  for a total of 25 intervals. The  $G'$  and  $G''$  versus shear strain graph was then produced based on the results.

## **3.5 Specimen Preparation**

To prepare specimens for mechanical testing, different solid loading of the feedstocks were used to 3D print various types of specimens. These specimens will subsequently undergo debinding and sintering processes to produce dense and solid ceramic-based AM components. The dimensions of the samples that were mechanically tested were described in Section 3.6, which was determined using the appropriate ASTM standard for ceramic materials. Moreover, since the printed samples will shrink during the sintering process, the size of the debound samples were smaller than the 3D-printed green sample. Several samples were produced for debinding and sintering, and the average sinkage was examined in the build directions and build plane. The CAD model of the sample will then be scaled up to correct for sinkage and meet the ASTM standard size.

### **3.5.1 Printing of Green Body**

Before printing the green body, the CAD model of the specimen was designed in Solidworks based on the shape and dimensions specified in Section 3.6 and saved as an STL file. The 3D model was sliced using PrusaSlicer to generate G-code for the 3D printer. In addition, other printing parameters were set using PrusaSlicer based on Table 3.1, including a constant extrusion temperature of 110 °C, bed temperature of 80 °C, 0.3 mm layer thickness, linear infill pattern,

and 100% infill density. The detailed slicer settings can be found in Appendix C. The samples were printed using a BIQU B1 3D printer with a customised pallet feedstock extruder head as in Appendix D, following the generated G-code. Finally, the mass of the printed green sample was measured using a weighing machine.

Table 3.1: Variable of Printing Parameter

Variable	Variable 1	Variable 2
Printing Parameter		
Build Orientation	Flat	On-edge
Raster angle	0°/90°	45°/-45°

### 3.5.2 Debinding

There were two steps in the debinding process: solvent debinding and thermal debinding. For solvent debinding, three different types of chemical solvents were used in this study: cyclohexane, turpentine, and N-heptane. The purpose of this was to investigate the influence of a chemical solvent on a sintered object's mechanical characteristics, grain size, crystal structure, and density. The chemical solvent dissolved the PW and SA in the green body. The green body sample was immersed in the chemical solvent for four hours and then air-dried at room temperature for at least three days to ensure the solvent was completely evaporated. In addition, the sample should be covered during the drying process, as cracking will occur when the solvent evaporated rapidly. The solvent-debound sample was weighed to ensure that the PW and SA were sufficiently removed from the green body (Huang, et al., 2021).

After that, the samples were sent to the furnace for thermal debinding, which can precisely be controlled by the heating temperature to remove the remaining PW, SA, and backbone binder, LDPE. The temperature was selected based on the TGA results in Section 3.3, with varying rates of increasing temperature to avoid sample cracking due to thermal shock and binders' degradation. The samples were heated from room temperature to 140 °C using a heating rate of 3 °C/min and held for 30 minutes when reached the desired temperature. Next, the heating temperature was increased to 600 °C using a

heating rate of 0.2 °C/min and held for 30 minutes when reached the desired temperature. Then, the samples were undergoing a pre-sintering process by heating the sample to 1000 °C using a heating rate of 10 °C/min. Lastly, the heating temperature was held for 30 minutes and then cooled down to room temperature by turning off the furnace. The purpose of the pre-sintering process was to slightly increase the mechanical properties to prevent damaging of the sample when moved to the sintering furnace since all the backbone binder has been removed. The overall thermal debinding and pre-sintering profile are shown in Figure 3.1.

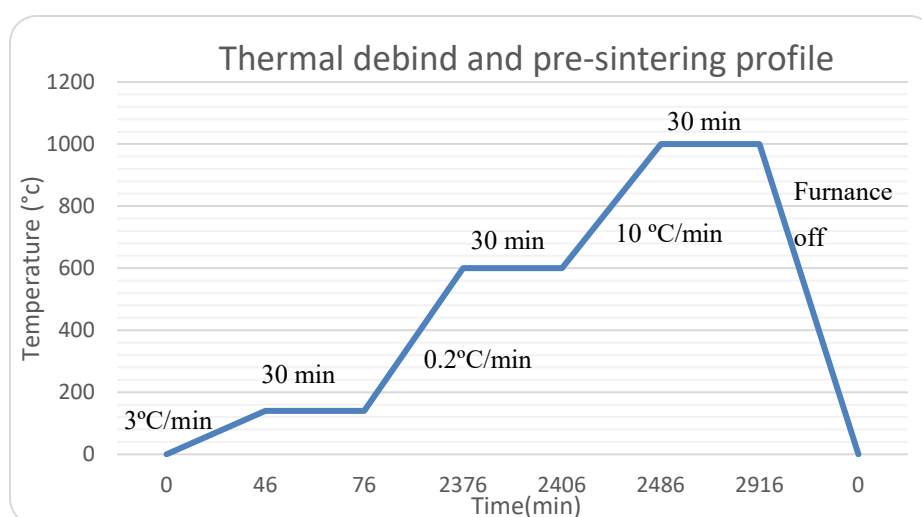


Figure 3.1: Graph of thermal debind and pre-sintering profile

### 3.5.3 Sintering

After cooling down from the pre-sintering process, the samples were transferred to the sintering furnace, which had a higher maximum operating temperature. The samples were heated to the sintering temperature of zirconia, which was 1500 °C, at a heating rate of 10 °C/min. A holding time of 2 hours was maintained at the desired temperature to carry out the sintering process. After completion, the samples were cooled to room temperature. Finally, the mass of the samples were measured, and the density was determined using the Archimedes method to ensure the production of a nearly dense zirconia AM part. The overall heating profile of the sintering process is shown in Figure 3.2.

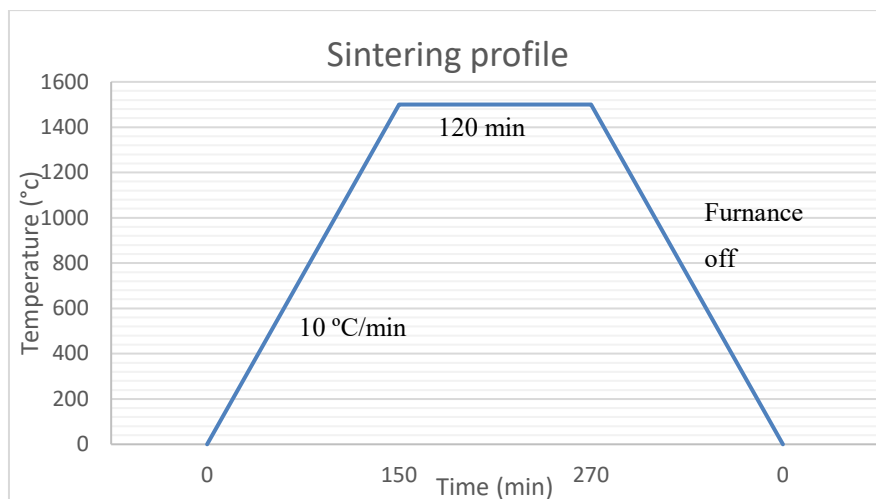


Figure 3.2: Graph of sintering profile

### 3.6 Density Test

The bulk density of the sintered zirconia samples were measured using the Archimedes method. A weighing machine with a density kit, along with distilled water as the immersion fluid, was used to obtain the density. The temperature of the water was maintained at 27 °C to determine the fluid density and increase the accuracy of the results. The samples were first measured in air and then in distilled water. The bulk density and relative density can be calculated using Equation 3.4 and Equation 3.5, respectively.

$$\rho_b = \frac{\rho_{fl@27^\circ C} W_a}{W_a - W_{fl}} \quad (3.4)$$

$$\rho_{Re} = \frac{\rho_b}{\rho_{ZrO_2}} \times 100\% \quad (3.5)$$

where

$\rho_b$  = bulk density, g/cm<sup>3</sup>

$\rho_{fl@27^\circ C}$  = density of distilled water at 27 °, g/cm<sup>3</sup>

$\rho_{ZrO_2}$  = density of zirconia, g/cm<sup>3</sup>

$W_a$  = sample's weight in air, g

$W_{fl}$  = sample's weight in distilled water, g

### 3.7 Scanning Electron Microscope

SEM (S-3400N, Hitachi) were used to study the surface morphology of the sintered sample by measuring the grain size. The samples were grinded using a grinding machine with P180 to P3000 silicon carbide waterproof sandpaper. During the grinding process, the sample were rotated 90 degrees when the grits of sandpaper are changed. As a guideline during the grinding process, the scratch lines from the last grit of sandpaper needed to be removed before moving to the next level of sandpaper. After that, the samples were polished using 5.0  $\mu\text{m}$  diamond paste followed by 1.0  $\mu\text{m}$  to ensure that the surface was smooth, flat, and free of scratches as in Appendix E. Next, the polished samples were sent to a furnace for thermal etching at 1450  $^{\circ}\text{C}$  with a heating rate of 10  $^{\circ}\text{C}/\text{min}$  and a holding time of 30 min once the desired temperature is reached. The thermal etching process was used to enhance the visibility of the grain boundaries. Finally, the samples were coated with a thin layer of a mixture of gold and vanadium as in Appendix E using a sputter coater, and the samples were ready to be observed using SEM. The coating served to preserve the original surface morphology, provided a conductive surface for the electron beam to interact, and reduced the charging effects to improve the resolution of the image capture.

In this test, a total of five types of specimens were observed by varying the solid loading (60 vol%, 65 vol%, 68 vol%) and the chemical solvent used during solvent debinding (cyclohexane, turpentine, N-heptane) to investigate their effect on grain size. The images were captured at an accelerating voltage of 15.0 kV using magnifications ranging from 1.0 k to 15.0 k. The grain size of the samples can then be measured by referring to the images.

### 3.8 X-ray Diffraction Analysis

XRD patterns of the sintered samples were obtained using an X-ray diffractometer (XRD-6000, Shidmazu) to study the crystal structure of the specimens. The diffraction patterns were obtained within  $2\theta$  from  $20^{\circ}$  to  $70^{\circ}$  with a measuring step of  $0.02^{\circ}$  and a measuring speed of 2 deg/min. An intensity vs  $2\theta$  graph was then plotted to obtain the XRD pattern of the specimens. In this test, a total of five types of specimens were tested by varying the solid loading (60 vol%, 65 vol%, 68 vol%) and the chemical solvent used during solvent



debinding (cyclohexane, turpentine, N-heptane) to investigate their effect on the crystal structure. Additionally, the XRD pattern of sintered zirconia formed using pure zirconia powder through die casting was tested as a reference. The XRD pattern of each type of specimen was compared to the reference, and the crystal structure of the specimens were determined.

### 3.9 Mechanical Testing

To investigate the mechanical performance of the specimens in terms of tensile strength, compressive strength, flexural strength, and hardness, various mechanical tests were performed. The appropriate equipment and testing specimens were utilized in accordance with the relevant ASTM standard. The factors that were studied include zirconia ceramic solid loading, chemical solvent used in solvent debinding, build orientation, and raster angle. Mechanical testing was performed on seven types of combination specimens, as shown in Table 3.2.

Table 3.2: Type of Specimen

Specimen	Solid Loading	Chemical solvent	Build orientation	Raster angle	Nozzle Diameter
1	60	Cyclohexane	Flat	0°/90°	0.4
2	65	Cyclohexane	Flat	0°/90°	0.4
3	68	Cyclohexane	Flat	0°/90°	0.4
4	65	Turpentine	Flat	0°/90°	0.4
5	65	N-Heptane	Flat	0°/90°	0.4
6	65	Cyclohexane	Flat	45°/-45°	0.4
7	65	Cyclohexane	On-edge	0°/90°	0.4

#### 3.9.1 Tensile Testing

By referring to ASTM C1273, tensile testing was performed at room temperature using a dog bone-shaped sample. As shown in Figure 3.3, the dimensions of the sample was slightly scaled down compared to the standard size to prevent warping and bending issues during the printing and sintering process. All types of specimens except for type seven in Table 3.3 was produced

and tested to examine their influence on tensile strength. Type seven specimens were excluded due to the difficulty of printing bridge structures. The grip section of the sintered tensile test samples were glued to an aluminum plate using epoxy to prevent the sample from breaking during clamping prior to testing. Tensile testing was performed using a Universal Testing Machine (AGS-100kNX, Shimadzu) with a 100 kN load cell and a constant displacement rate of 1 mm/min. Following the test, a stress-strain graph was drawn to determine the ultimate tensile strength using Equation 3.6. Each specimen type was examined three times to determine the average and standard deviation of ultimate tensile strength.

$$\sigma_{tensile} = \frac{P}{A} \quad (3.6)$$

where

$P$  = tensile force, N

$A$  = gage's cross section area, mm<sup>2</sup>

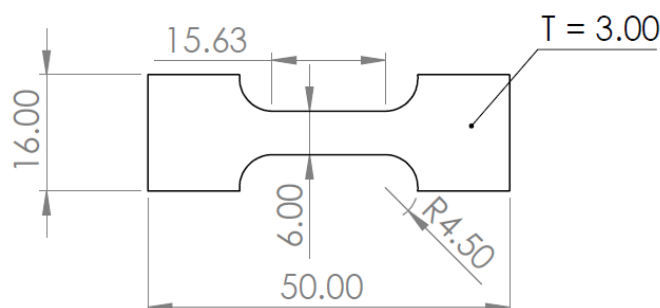


Figure 3.3: Dimension of Dog Bone Shape Sample for Tensile Test

### 3.9.2 Flexural Testing

The three-point bend test examined the flexural strength at room temperature using a rectangular bar shape of 32 mm in length, 13 mm in width, and 6 mm in thickness. Type one to type six of specimens in Table 3.3 were fabricated and tested to evaluate the influence on flexural strength. Based on ASTM C1273, a Universal Testing Machine (AGS-100kNX, Shimadzu) universal testing machine with a 100 kN load cell and a constant displacement rate of 0.1 mm/min was used for the flexural test. Cylindrical rollers with a span of 25 mm were used for support, and the sample was loaded at the centre until it breaks to record the breaking force. Following the test, a stress-strain graph was plotted to

determine the ultimate flexural strength using Equation 3.7. Furthermore, each specimen type were examined three times to determine the average and standard deviation of ultimate flexural strength.

$$\sigma_{bend} = \frac{3FL}{2Wt^2} \quad (3.7)$$

where

$F$  = bending load, N

$L$  = length of support span, mm

$W$  = sample's width, mm

$t$  = sample's thickness, mm

### 3.9.3 Compressive Testing

To analyse the material's compressive strength, a cylindrical form specimen with 6.35 mm diameter and 12.70 mm height was selected for the compression test using ASTM C1424. Because similar samples were manufactured in cylindrical form with varied raster angles. As a result, specimens type six, which vary the raster angle, was excluded for compressive strength. A total of six different types of specimens were fabricated and tested to study the influence on compressive strength in Table 3.3. The test was performed using Universal Testing Machine (AGS-100kNX, Shimadzu) equipped with a 100 kN load cell and a constant displacement rate of 1 mm/min. Following the test, a stress-strain graph was sketched to determine the maximum compressive strength using Equation 3.8. Furthermore, each specimen type was examined three times to determine the average and standard deviation of maximum compressive strength.

$$\sigma_{comp} = \frac{P_{max}}{A} \quad (3.8)$$

where

$P$  = compressive load, N

$A$  = sample's cross section area, mm<sup>2</sup>

### 3.9.4 Hardness Testing

The Vickers hardness test was used to evaluate the hardness of specimens according to ASTM C1327. Since altering build orientation, raster angle, and nozzle diameter have no significant influence on hardness, only specimens one to five in Table 3.3 were fabricated and tested to study their effect on hardness. The Vickers hardness test was performed using a Vickers hardness tester and a diamond indenter. A 10 kg load force was applied for a dwell time of 10 seconds. The indentation area was measured, and the Vickers hardness numbers were calculated using Equation 3.9. Fifteen indentations were performed on each type of specimen, and each type of specimen was fabricated three times. Finally, the average and standard deviation of the Vickers number was calculated.

$$HV = 1854.4 \frac{F}{L^2} \quad (3.9)$$

where

$HV$  = Vickers number

$F$  = load force, N

$L$  = indentation's diagonal length, mm

### 3.10 Work Breakdown Structure

Figure 3.4 shows the work breakdown structure for FYP 1 and FYP 2.

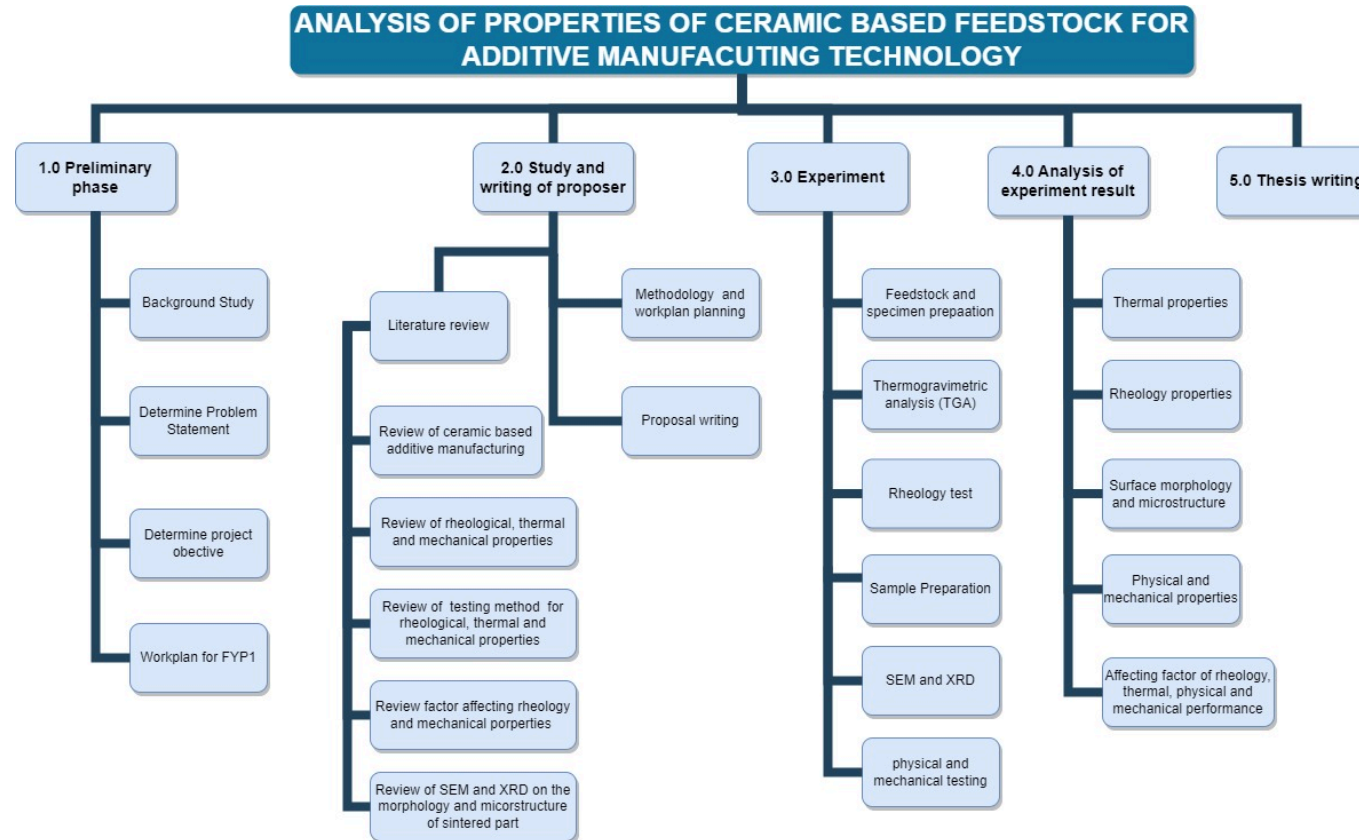


Figure 3.4: Work Breakdown Structure of Project

## CHAPTER 4

### RESULTS AND DISCUSSION

#### 4.1 Introduction

The properties of different types of feedstock and sintered specimens had been analysed through a series of tests to determine the effect of solid loading, debinding solvent, and printing parameters. The optimal solid loading, debinding solvent, and printing parameters were determined and used for future ceramic-based 3D printing. The result that will be discussed in this chapter are:

- (i) Thermal Properties of Feedstock
- (ii) Rheological Properties of Feedstock
- (iii) Scanning Electron Microscope
- (iv) X-ray Diffraction Analysis
- (v) Physical Properties of Sintered Specimen
- (iv) Mechanical Properties of Sintered Specimen

#### 4.2 Thermal Properties of Feedstock

The thermal properties of feedstocks with different solid loading (60 vol%, 65 vol%, and 68 vol%) were analysed through TGA. Figures 4.1, 4.2, and 4.3 show the TGA results of feedstocks with 60 vol%, 65 vol%, and 68 vol% solid loading, respectively. Based on the derivative weight of these figures, it is evident that all three types of feedstocks were thermally stable up to about 140 °C, beyond which the binder started to degrade. Furthermore, all three types of feedstocks exhibited two stages of decomposition during TGA. PW and SA began to decompose at around 140 °C, while LDPE started to decompose at around 400 °C, with increasing temperature. Therefore, the printing temperature must be kept below 140 °C to ensure that the printed green sample is reusable without decomposition of the binder. Additionally, the binder in all three types of feedstocks was completely decomposed at 550 °C. The only difference in the TGA curves of the feedstocks was the amount of zirconia remaining, which was 88.01 wt%, 89.56 wt%, and 90.53 wt% for 60 vol%, 65 vol%, and 68 vol% solid loading, respectively. This is because the more zirconia solid loading in a feedstock, the more zirconia will remain after the binders are removed. In

addition, based on the heat flow profile in the TGA results of the feedstocks, it was observed that all three types of feedstocks exhibited similar endothermic phase transition temperatures. PW and SA in the feedstock began to melt in the range of 56 °C to 59 °C, while LDPE began to melt in the range of 93 °C to 95 °C. Thus, the melting point of the binder was slightly different from their individual melting points, which were 52 °C for PW, 70 °C for SA, and 110 °C for LDPE. This indicates that all components interacted with each other to some extent, but not completely dissolved, which is similar to the findings of Huang, et al. (2021).

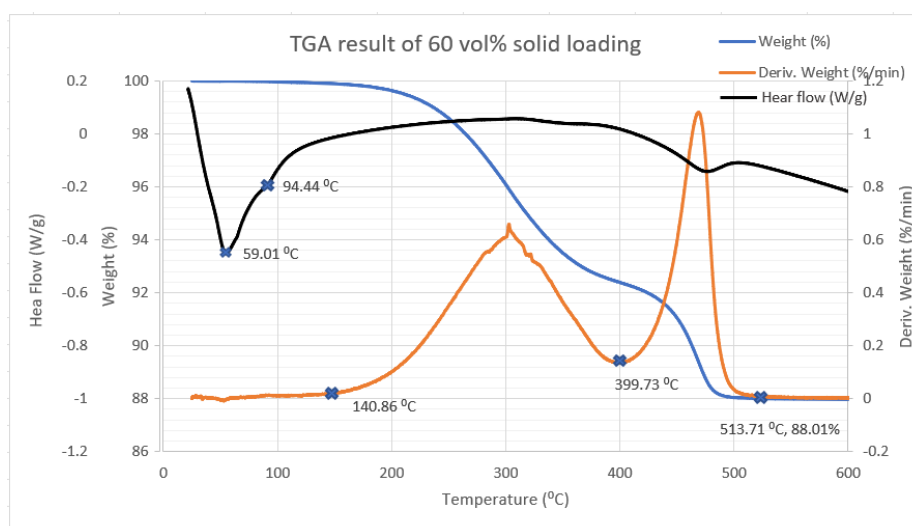


Figure 4.1: Thermal properties of 60 vol% zirconia feedstock

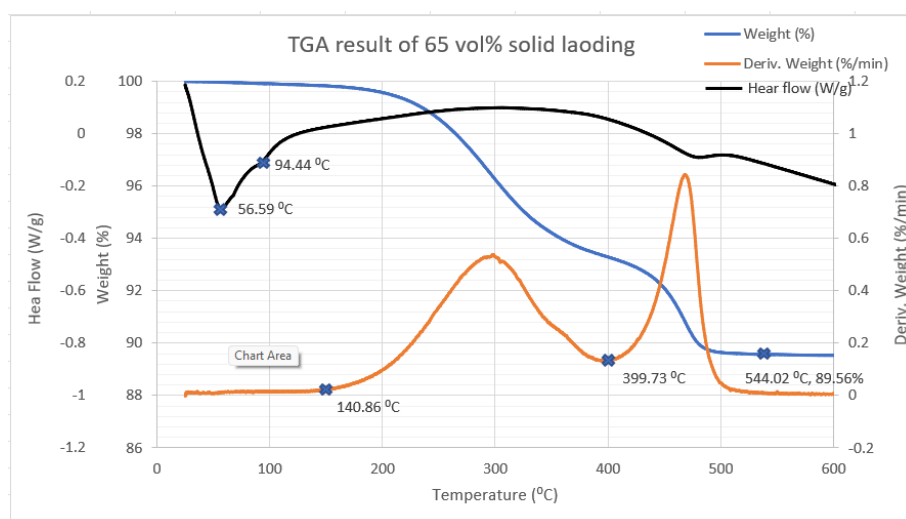


Figure 4.2: Thermal properties of 65 vol% zirconia feedstock

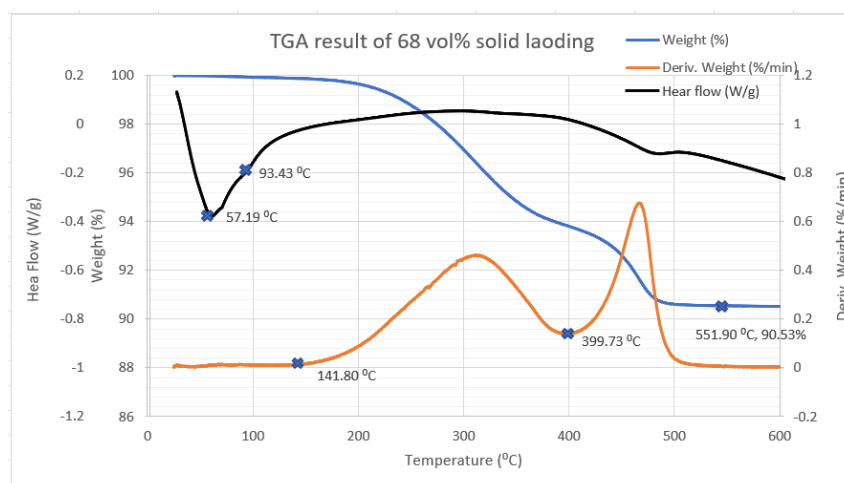


Figure 4.3: Thermal properties of 68 vol% zirconia feedstock

### 4.3 Rheological Properties of Feedstock

The rheological behaviour of the feedstock with different solid loading (60 vol%, 65 vol%, 68 vol%) was analysed using a rheometer. Two types of tests were conducted to study the rheology behaviour: viscosity test and oscillatory strain sweep.

#### 4.3.1 Viscosity Test

In the viscosity test, the viscosity of the feedstocks was measured by increasing the shear rate to determine whether the feedstock behaves as a Newtonian or non-Newtonian fluid when heated. The same test was repeated at different temperatures to study the impact of temperature on the viscosity of the feedstocks. Figure 4.4, Figure 4.5, and Figure 4.6 show the viscosity test results of feedstocks with 60 vol%, 65 vol%, and 68 vol% solid loading, respectively. All three types of feedstocks exhibited shear thinning (pseudoplastic) behaviour which the viscosity will decrease with shear rate, and the viscosity decreased as the temperature increased. Therefore, the feedstock can be extruded through the nozzle with minimal extrusion force, as the viscosity gradually decreases when subjected to small increases in shear rate. Additionally, the extrusion temperature can be varied from 100 °C to 140 °C to decrease the viscosity of the feedstock. Furthermore, the feedstocks showed the same viscosity behavior as other researchers' ceramic-based feedstocks for piston-based material extrusion done by Huang, et al. (2021) and silicon carbide ceramic-based feedstock for powder and slurry-based 3D printing done by Masuda, Ohta, and Kitayama



(2019). Moreover, the viscosity of the feedstock decreased as the solid loading increased from 60 vol% to 68 vol%. This is because when the solid loading increases, the amount of binder, especially PW, which acts as a plasticizer to reduce the viscosity, decreases.

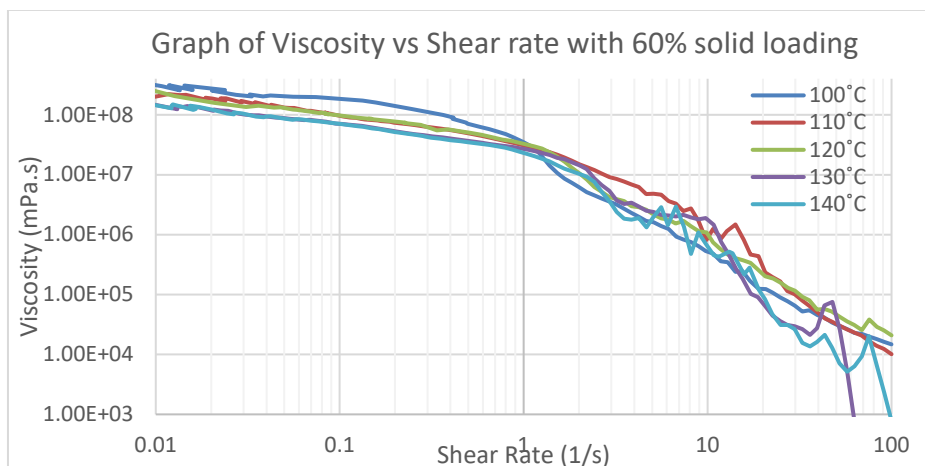


Figure 4.4: Graph of Viscosity Test Result of 60 vol% Solid Loading

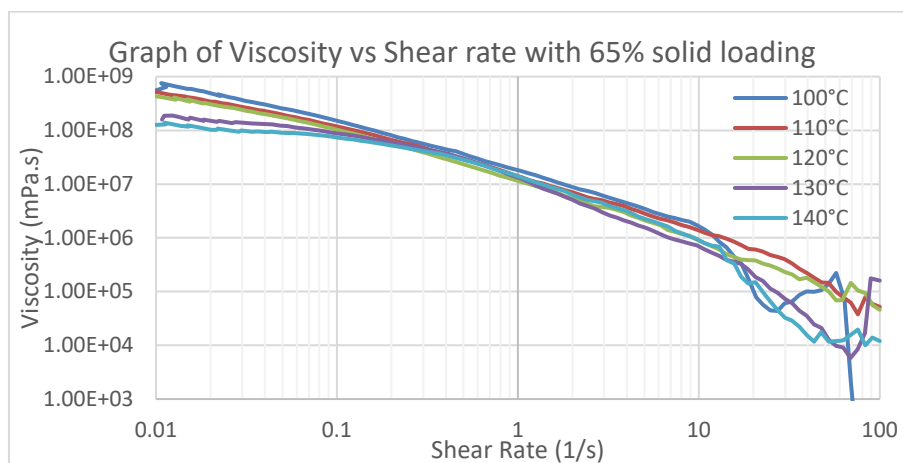


Figure 4.5: Graph of Viscosity Test Result of 65 vol% Solid Loading

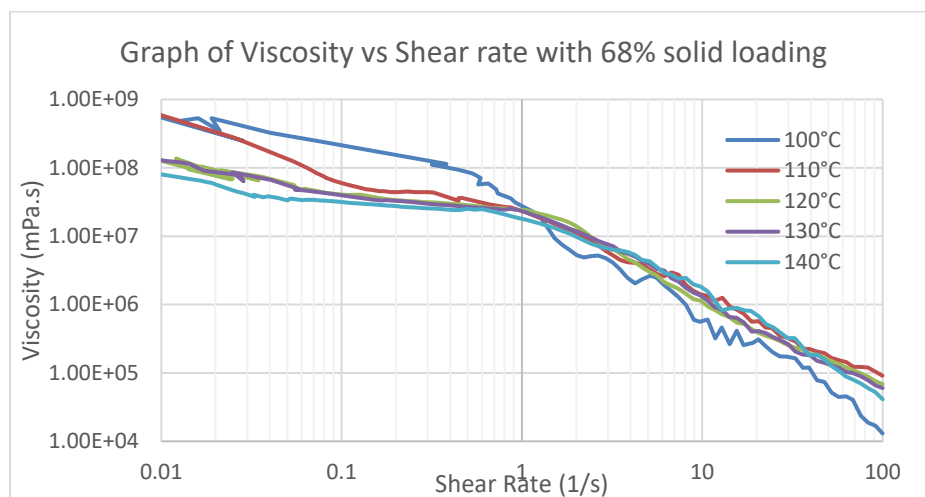


Figure 4.6: Graph of Viscosity Test Result of 68 vol% Solid Loading

### 4.3.2 Oscillatory strain sweep

In this test, the  $G'$  and  $G''$  of the feedstocks were measured by increasing the shear strain from 0.01 % to 100 % at a constant temperature of 110 °C and constant angular frequency of 6.28 rad/s. The reason for conducting this test was to determine the linear viscoelastic range, critical oscillatory strain, and shear yield strain of the feedstocks. Figure 4.7, Figure 4.8, and Figure 4.9 show the viscosity test results of feedstocks with 60 vol%, 65 vol%, and 68 vol% solid loading, respectively. By referring to the figures, it shows similar characteristics in all three types of feedstocks. Both  $G'$  and  $G''$  were independent of the shear strain and remained constant when the shear strain was below around 0.1%. Therefore, the viscoelastic range of all three types of feedstocks is similar when the shear strain is less than 0.1 %, and the critical oscillatory strain is equal to 0.1 % of the shear strain. When the shear strain was larger than the critical oscillatory strain, both  $G'$  and  $G''$  started to decrease. In addition, when the shear strain keeps increasing,  $G'$  will be the same as  $G''$  when the shear strain was called the shear yield strain. The feedstock undergoes a transition from a solid-like state to a liquid-like state as the  $G'$  is lower than  $G''$  beyond the shear yield strain. In 60 vol%, 65 vol%, and 68% solid loading, the shear yield strains were 0.678 %, 0.314 %, and 0.680 %. Therefore, there was a minimal effect on the linear viscoelastic range as well as the critical oscillatory strain when varying the solid loading. However, the solid loading will affect the shear yield strain in the range from 0.314 % to 0.680 %.

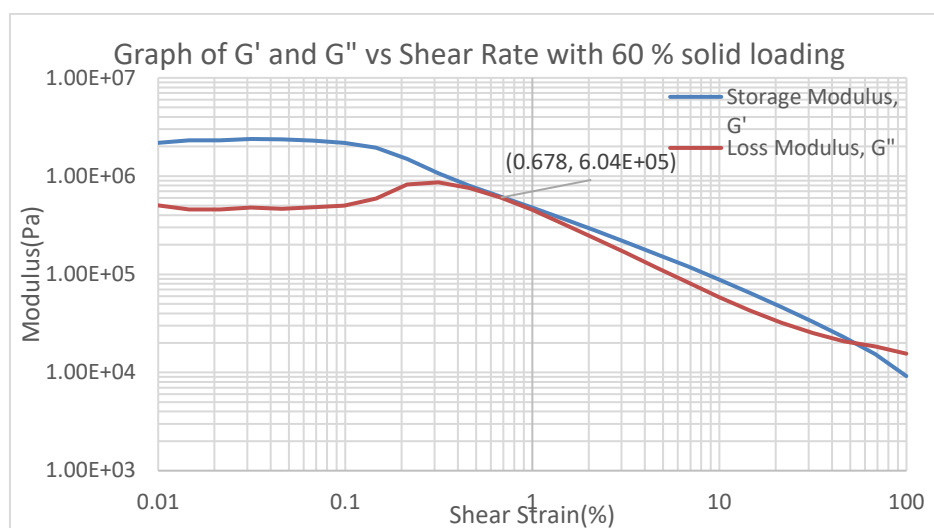


Figure 4.7: Graph of Oscillatory Strain Sweep of 60 vol% Solid Loading

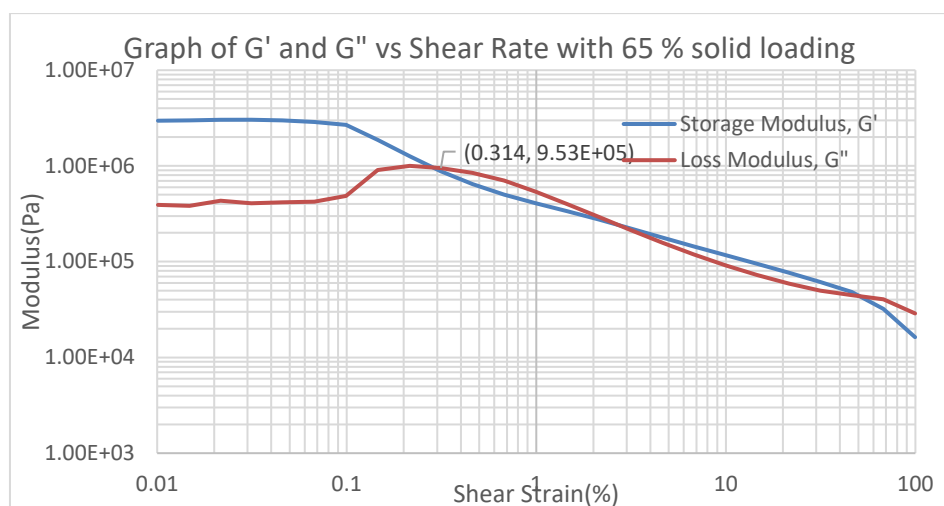


Figure 4.8: Graph of Oscillatory Strain Sweep of 65 vol% Solid Loading

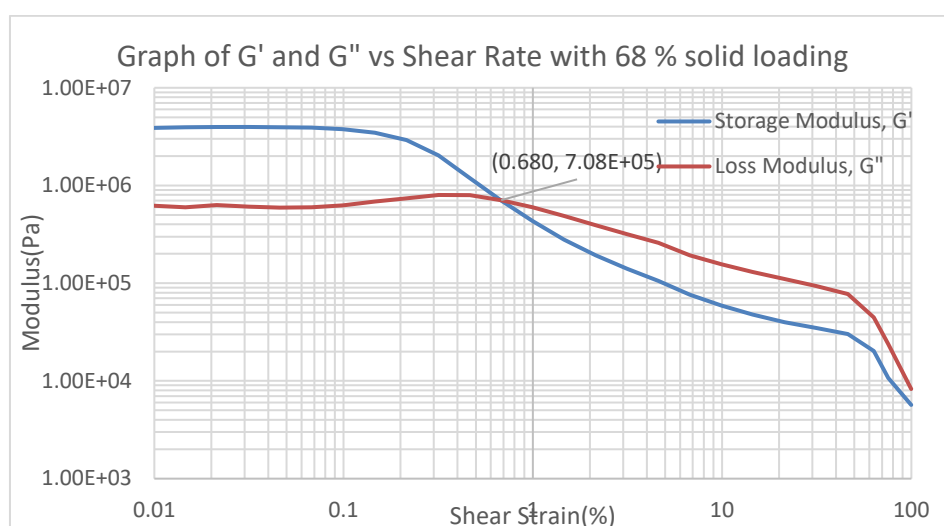


Figure 4.9: Graph of Oscillatory Strain Sweep of 68 vol% Solid Loading

#### 4.4 Scanning Electron Microscope

The surface morphology of sintered specimens with different solid loadings (60 vol%, 65 vol%, 68 vol%) and solvents used in solvent debinding (cyclohexane, turpentine, N-heptane) can be analyzed using SEM. Grain size and pore size in the sintered specimens were measured and observed using SEM. Figure 4.10 shows images of the different specimens captured at 1k, 5k, and 15k magnifications. The default solid loading and solvent used in solvent debinding were 65 vol% and cyclohexane, respectively. Figures 4.10a, 4.10b, and 4.10c were used to compare the effect of solid loading on the surface morphology, while Figures 4.10b, 4.10d, and 4.10e were used to compare the effect of solvent debinding. In terms of solid loading, there were fewer pores observed in the

specimen with a solid loading of 65 vol% compared to those with 60 vol% and 68 vol%. In contrast, in terms of solvent, specimens debound using turpentine resulted in fewer pores compared to those debound using cyclohexane. Moreover, no binder could be observed through SEM in the sintered specimens, indicating that the binder had been completely removed. The microstructure of all the sintered specimens was crystalline solid form.

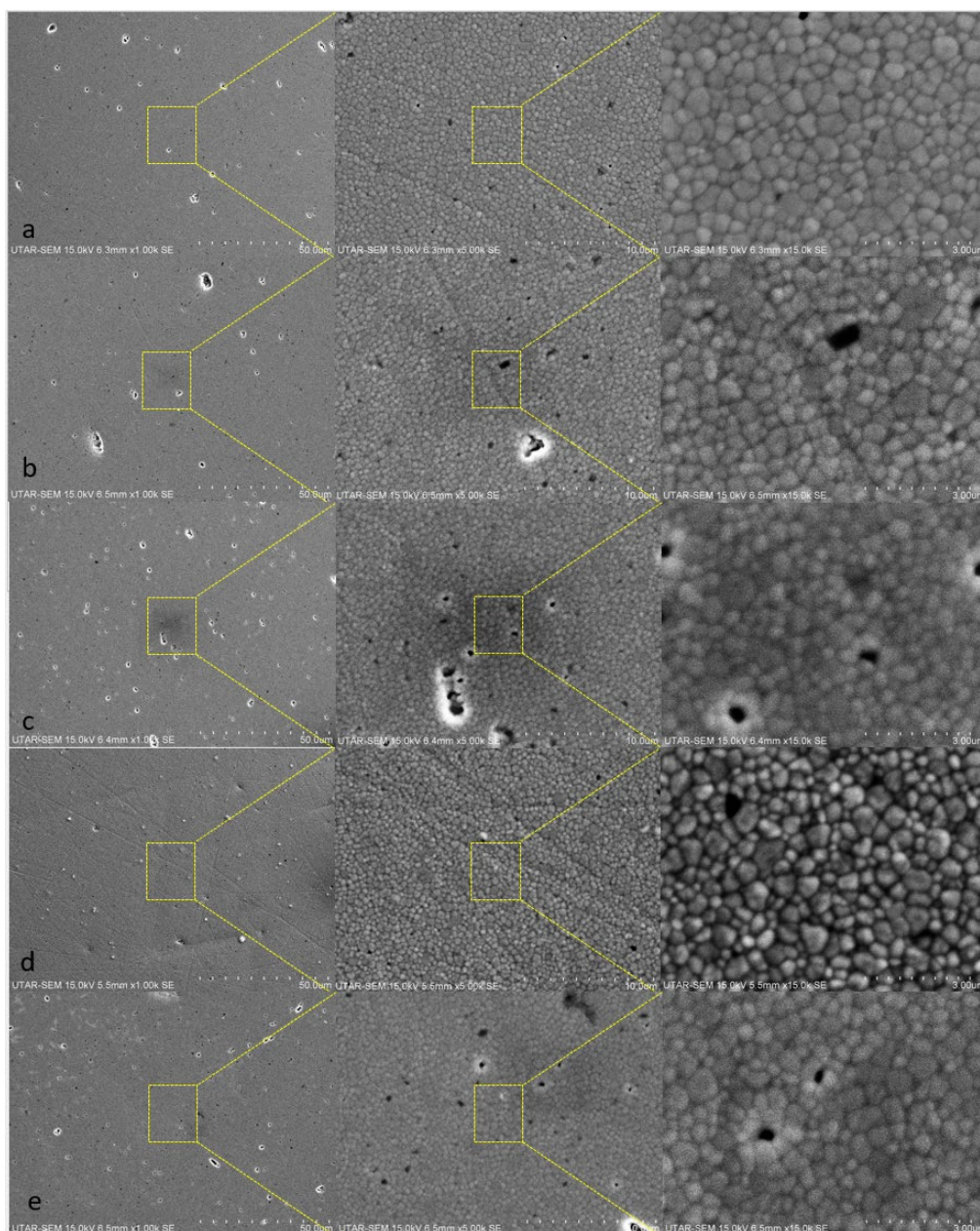


Figure 4.10: SEM morphology of polished and thermal etched sintered specimen under different magnification. (a) 60 vol%, cyclohexane (b) 65 vol%, cyclohexane (c) 68 vol%, cyclohexane (d) 65 vol%, Turpentine (e) 65 vol%, N-heptane

In addition, the average grain size of the sintered specimens was measured under 15k magnification. Referring to Table 4.1, it shows that the grain size for all the specimens were similar hovering around  $0.4 \mu\text{m}$ . Specimen with 68 vol% solid loading had the smallest grain size,  $434 \pm 20.7 \text{ nm}$ , while those with 60 vol% and 65 vol% solid loading had the same average grain size,  $444 \text{ nm}$ . Thus, solid loading has a minor effect on the grain size of the sintered specimen by decreasing the grain size when solid loading increases. Furthermore, turpentine used as the solvent in solvent debinding resulted in the smallest grain size,  $426 \pm 31.4 \text{ nm}$ , followed by N-heptane,  $430 \pm 25.4 \text{ nm}$ , and cyclohexane,  $444 \pm 33.4 \text{ nm}$ . Therefore, it shows that the grain size of the sintered specimens was slightly affected when the solvent used in solvent debinding was varied, and the strength of the specimens were also affected.

Table 4.1: Table of average grain size of sintered specimen with different solid loading and solvent

Type of specimen		Average grain size (nm)
Solid loading (vol%)	Solvent	
60	Cyclohexane	$444 \pm 27.2$
65	Cyclohexane	$444 \pm 33.4$
68	Cyclohexane	$434 \pm 20.7$
65	Turpentine	$426 \pm 31.4$
65	N-heptane	$430 \pm 25.4$

#### 4.5 X-ray Diffraction Analysis

The crystalline structure and orientation of sintered specimens with different solid loading (60 vol%, 65 vol%, 68 vol%) and solvents used in solvent debinding (cyclohexane, turpentine, N-heptane) were determined and compared using XRD patterns obtained from  $20^\circ$  to  $70^\circ$ . A total of 5 types of sintered specimens were studied, with 65 vol% solid loading and cyclohexane as the default solid loading and solvent for solvent debinding, respectively. Additionally, sintered zirconia formed by using pure zirconia powder through die casting was used as the reference sample. Figure 4.11 shows that the XRD patterns of the specimens have similar peak intensities at the same  $2\theta$  angles, indicating that all types of specimens have similar zirconia structures. This is because zirconia doped with yttria stabilizes the structure (Neacsu, et al., 2016).

The solvents used in solvent debinding mainly change the connection between binders and zirconia particles, without affecting the zirconia phase composition (Li, et al., 2020). The crystalline structure of all sintered specimens was mainly tetragonal, which was the same as the reference sample. The tetragonal crystal structure of zirconia had the dominant miller index (1,0,1) orientation of crystal plane, with the highest peak intensity at around  $2\theta = 30.24^\circ$ . This is consistent with the phase diagram of yttria-stabilized zirconia, which shows that zirconia doped with 3 mol% of yttria will have a tetragonal crystal structure when heated at 1500 °C, as shown in Figure 4.12.

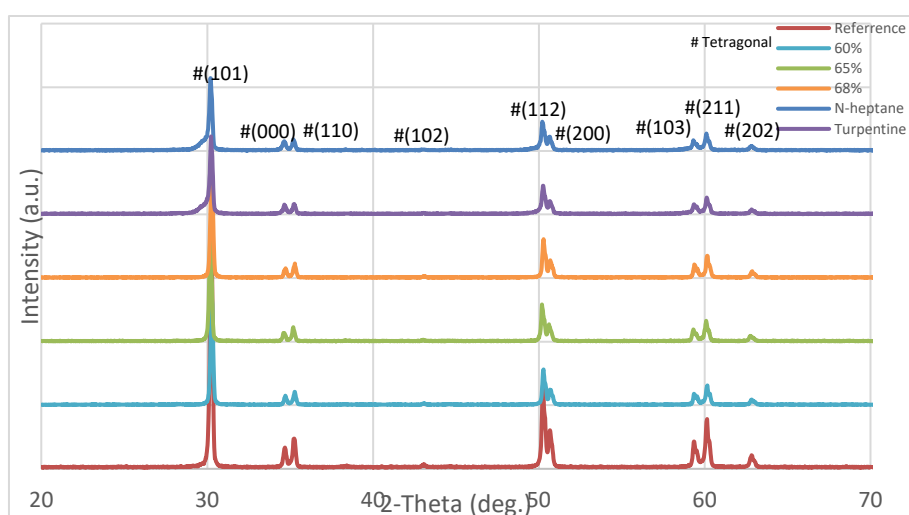


Figure 4.11: XRD pattern of sintered zirconia with different solid loading and solvent debind

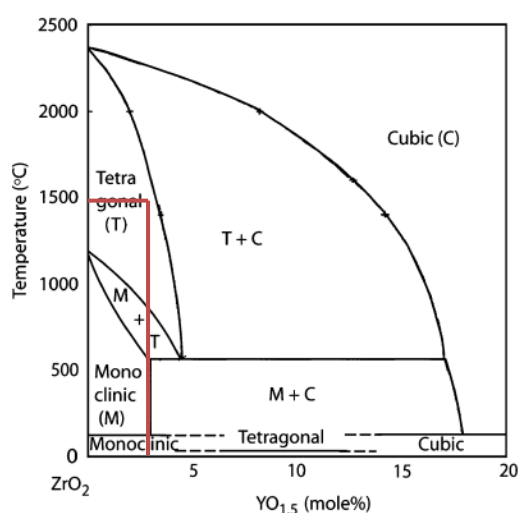


Figure 4.12: Phase diagram of yttria-stabilized zirconia at 3 mol% yttria, 1500 °C (Witz et al., 2007)

## 4.6 Physical Properties of Sintered Specimen

In this research, the specimens for mechanical testing were printed as stated in Section 3.9, followed by solvent debinding, thermal debinding, and sintering. Therefore, physical properties of the feedstock in terms of shrinkage, weight loss, and density were determined by measuring the mass and dimensions of the green sample, solvent debound sample, and sintered sample. Some examples of the samples are shown in Appendix F.

### 4.6.1 Shrinkage of Sintered Specimen

The printed green zirconia samples undergo shrinkage during the sintering process due to the reduction of porosity and densification, which enhances the mechanical properties of the specimens. Figure 4.13 shows that the shrinkage of dimensions was measured and calculated for a total of five types of specimens with different solid loading (60 vol%, 65 vol%, 68 vol%) and solvents used in solvent debinding (cyclohexane, turpentine, N-heptane). The average dimension shrinkage of the samples decreases from  $18.47 \pm 0.92$  % to  $16.71 \pm 0.45$  % and  $15.14 \pm 0.62$  % when the solid loading increases from 60 vol% to 65 vol% and 68 vol%. This is due to the fact that the higher the solid loading, the more zirconia ceramic base material packs closely in the feedstock, resulting in lesser shrinkage during the sintering process.

However, there was no significant difference in the dimension shrinkage of the samples when varying the solvent used in solvent debinding between cyclohexane, turpentine, and n-heptane, which had  $16.71 \pm 0.45$  %,  $16.73 \pm 0.35$  %, and  $16.73 \pm 0.45$  % of shrinkage, respectively. This is because solvent debinding was done at room temperature and only removes a partial amount of the binder in the sample, while the temperature of the sintering process and thermal debinding was much higher, at 1500 °C and 600 °C, respectively. Therefore, the shrinkage of the specimens was dominant by the solid loading of the feedstock, while the solvent used in solvent debinding had no significant impact on it.



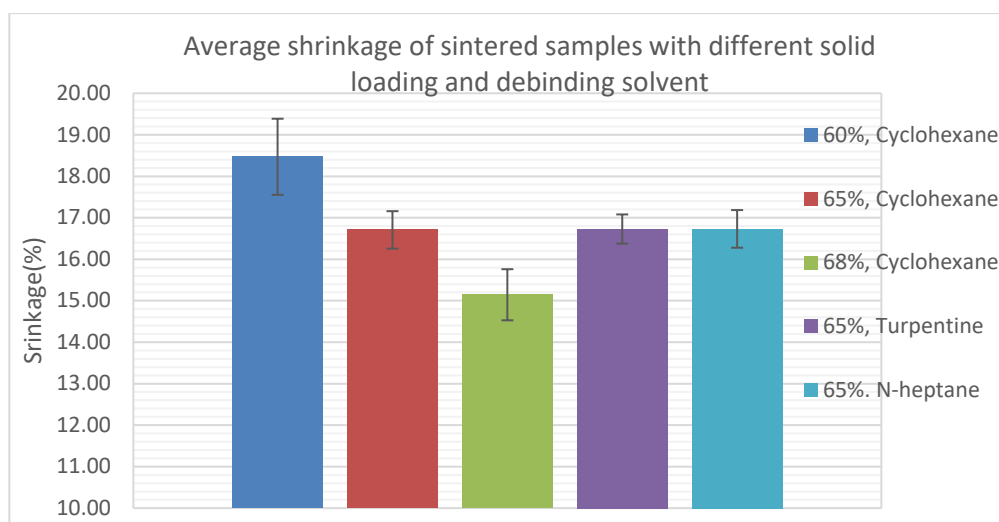


Figure 4.13: Bar chart of dimension shrinkage of sintered sample with different solid loading and debinding solvent

#### 4.6.2 Weight Loss of Solvent Debound and Sintered Specimen

In terms of weight loss, there was a significant difference in mass when comparing the mass of the green specimen, solvent-debonded specimen, and sintered specimen. This is because part of the soluble binders in the feedstock, which are PW and SA, were removed during solvent debinding, and the remaining PW, SA, and backbone binder were removed during thermal debinding, leaving only the zirconia ceramic loading in the specimen. Referring to Figure 4.14, it shows that the average weight loss of both the solvent-debonded and sintered specimens decreases as the solid loading increases. The solvent-debonded specimen in 60 vol%, 65 vol%, and 68 vol% had an average mass loss of  $2.88 \pm 0.88$  %,  $2.32 \pm 0.75$  %, and  $1.60 \pm 0.44$  %, respectively. This is because the weightage of soluble binder in the feedstock decreases as the solid loading increases, resulting in a lower concentration of soluble binder, which in turn results in less binder being removed during solvent debinding. Besides, the average weight loss of the sintered specimen in 60 vol%, 65 vol%, and 68 vol% had a weight loss of  $12.08 \pm 0.10$  %,  $10.50 \pm 0.13$  %, and  $9.76 \pm 0.24$  %, respectively. This is because a higher solid loading results in less binder present in the feedstock, and more zirconia ceramic will remain in the specimen after sintering. Additionally, the weight loss of the sintered specimen has similar results in Section 4.2, which is the TGA of feedstock, which were 11.99%,



10.44%, and 9.47% for 60 vol%, 65 vol%, and 68 vol% solid loading, respectively.

On the other hand, there was only a minor difference in weight loss between solvent debound and sintered specimens when varying the solvent used in solvent debinding. After solvent debinding, the average weight loss was  $2.32 \pm 0.75\%$  for cyclohexane,  $2.38 \pm 0.49\%$  for turpentine, and  $2.36 \pm 0.64\%$  for n-heptane. In sintered specimens using cyclohexane, turpentine, and n-heptane, the average weight loss was  $10.50 \pm 0.13\%$ ,  $10.42 \pm 0.13\%$ , and  $10.49 \pm 0.15\%$ , respectively. Thus, the weight loss of solvent debound and sintered specimens were predominantly influenced by the volume of solid loading and binders, while the solvent used in solvent debinding has minimal effect.

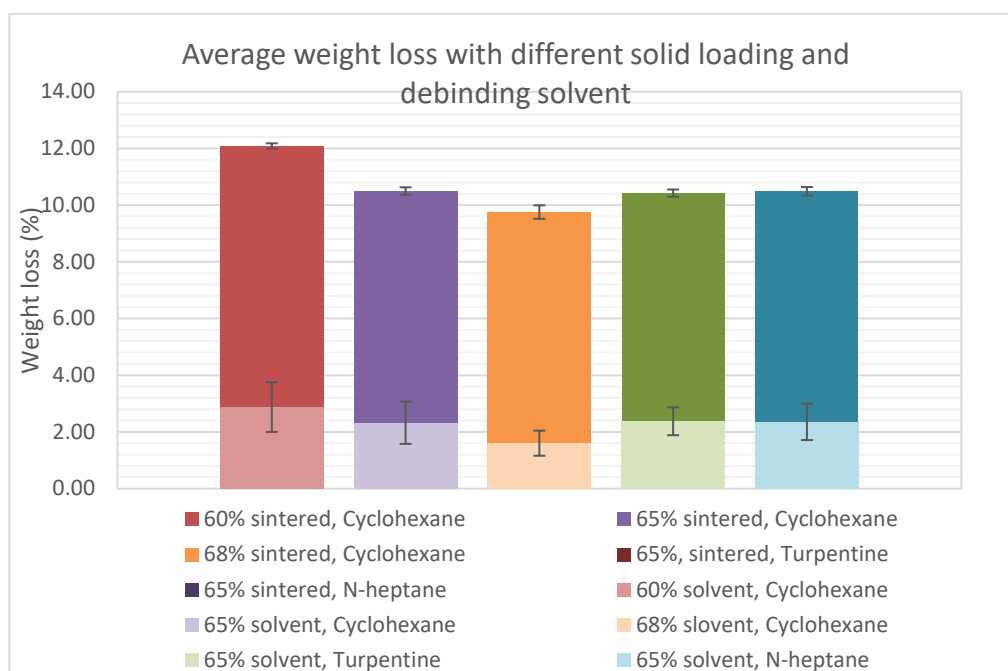


Figure 4.14: Bar chart of weight loss of sintered specimen with different solid loading and debinding solvent

### 4.6.3 Density of Sintered Specimen

Total of five types of specimens with different solid loading (60 vol%, 65 vol%, 68 vol%) and solvent used in solvent debinding (cyclohexane, turpentine, n-heptane) that were used to analyse the effect on the density of sintered specimens. Figure 4.15 shows the average bulk density of the sintered specimens. The specimen with 65 vol% solid loading had the lowest average

bulk density,  $5.85 \pm 0.08 \text{ g/cm}^3$ , while the specimens with 65 vol% and 68 vol% solid loading had the highest average bulk density,  $5.91 \pm 0.05 \text{ g/cm}^3$  and  $5.91 \pm 0.07 \text{ g/cm}^3$ , respectively. The higher density in the 60 vol% and 68 vol% solid loading specimens may be due to the cracking that occurred, as shown in Appendix G. Water was able to fill up the void in the sample during the measurement of the sample's mass in water by Archimedes' method, resulting in higher density. On the other hand, when varying the solvent used in solvent debinding, it was found that sintered samples using both turpentine and n-heptane as debinding solvents resulted in the highest average bulk density,  $5.89 \pm 0.05 \text{ g/cm}^3$  and  $5.89 \pm 0.04 \text{ g/cm}^3$ , respectively, while cyclohexane resulted in the lowest average bulk density,  $5.85 \pm 0.08 \text{ g/cm}^3$ . Thus, the bulk density of the sintered samples was affected by solid loading, but the accuracy of the result will be affected by cracking. The solvent used in solvent debinding will also affect the bulk density of the sintered specimen, although it had no influence on the weight loss and shrinkage.

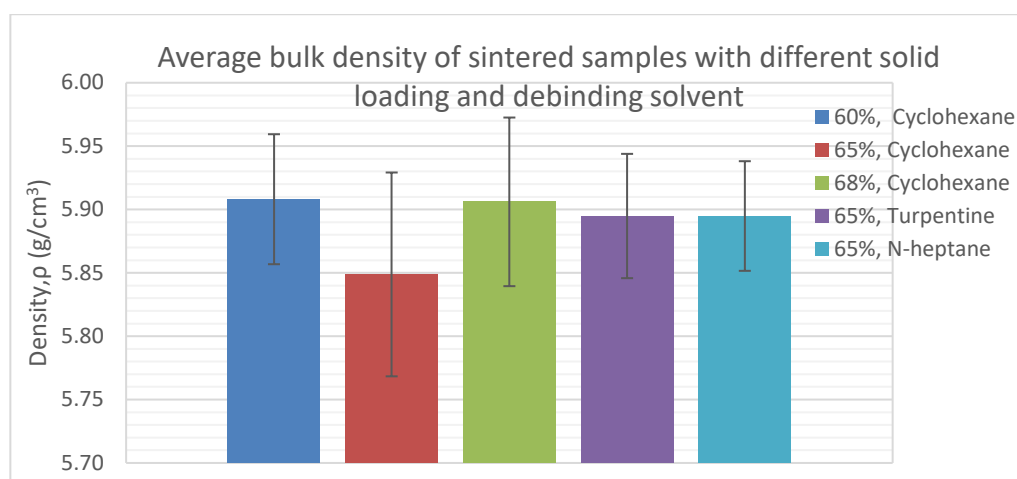


Figure 4.15: Bar chart of bulk density of sintered samples with different solid loading and debinding solvent

In addition, Figure 4.16 shows that the relative density of all sintered specimens were high, with an average relative density of more than 96.0% compared to the zirconia ceramic base material (KZ-3YF type C) which has a theoretical density of  $6.07 \text{ g/cm}^3$ . Therefore, the feedstocks with 60 vol%, 65 vol%, and 68 vol% solid loading are suitable for structural ceramics, as well as the solvents used in solvent debinding, which are cyclohexane, turpentine, and n-heptane (Pelz et al., 2021).

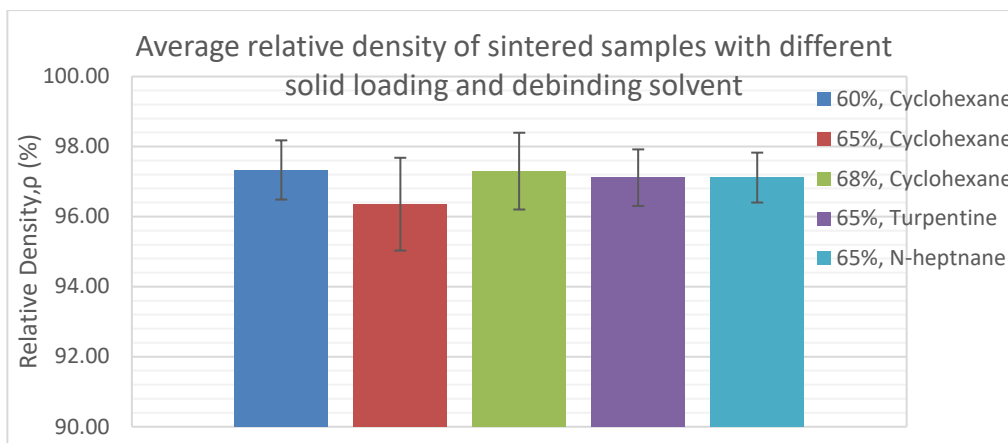


Figure 4.16: Bar chart of relative density of sintered specimen with different solid loading and debinding solvent

#### 4.7 Mechanical Properties of Sintered Specimen

After the sintering process, the mechanical properties of the sintered specimens were tested by using the methods described in Section 3.9, which involved measuring their relative shape and size. A total of four mechanical tests were conducted in this research to study their mechanical properties, including compressive test, bending test, tensile test, and Vickers hardness test. The mechanical strength of each type of specimen was compared to determine the best solid loading, debinding solvent, and printing parameters. Table 4.2 shows the types of specimens used in the mechanical tests.

Table 4.2 : Type of specimens

Specimen	Solid Loading	Chemical solvent	Build orientation	Raster angle	Nozzle Diameter
1	60	Cyclohexane	Flat	0°/90°	0.4
2	65	Cyclohexane	Flat	0°/90°	0.4
3	68	Cyclohexane	Flat	0°/90°	0.4
4	65	Turpentine	Flat	0°/90°	0.4
5	65	N-Heptane	Flat	0°/90°	0.4
6	65	Cyclohexane	Flat	45°/-45°	0.4
7	65	Cyclohexane	On-edge	0°/90°	0.4

### 4.7.1 Tensile Strength

The tensile test was conducted on dog-bone shaped sintered samples until fracture to determine their tensile strength. All types of specimens listed in Table 4.2, except for type seven, were used in the tensile test, as it was difficult to print the bridge structure required for that type. Appendix H shows that the majority of the fractures occurred at the gage section, which was the location where stress is concentrated. Although the grip section of the specimen was glued to an aluminum plate using epoxy to overcome bending and wrapping issues that occurred during printing and sintering as in Appendix I, some shaking moments of the tensile test jig during the gripping of the sample caused a large number of samples to break before the test started, due to the brittle nature of the ceramic material.

The tensile strength of different types of specimens was calculated from the test results and is shown in Table 4.3. Out of the eighteen tests conducted, nine were successful in obtaining the tensile strength of the specimens. The tensile strength of the sintered zirconia varied from 30.78 MPa up to 115.12 MPa. Although the tensile test was successful only once for type six specimens, which had a 45° raster angle, it showed a relatively low tensile strength compared to other types of specimens. Therefore, a 90° raster angle may provide the maximum tensile strength, which is consistent with the recent research by Huang, et al. (2021).

Table 4.3: Table of tensile test results with different sintered specimens

Number of tests Specimens	Tensile Strength (MPa)		
	1	2	3
1	failed	103.01	76.40
2	failed	failed	115.12
3	failed	failed	failed
4	109.20	102.31	56.22
5	103.50	failed	61.56
6	30.78	failed	failed

#### 4.7.2 Flexural strength

The bar-shaped samples were used to conduct three-point bend tests to determine the flexural strength of the specimens until fracture. The fractures of the three-point bend test specimens mostly occurred at the middle of the specimen, as shown in Appendix J. All types of specimens in Table 4.2, except type seven, were used in the three-point bend test. The average flexural strength of the different types of sintered specimens calculated from the test results is shown in Figure 4.17. In terms of solid loading, 65 vol% resulted in the highest average flexural strength of  $27.79 \pm 13.19$  MPa, followed by 60 vol% and 68% with  $25.67 \pm 19.44$  MPa and  $20.13 \pm 3.68$  MPa, respectively. This may be due to serious cracking occurring in the 60 vol% and 68 vol% solid loading specimens, while there is little cracking in the 65% solid loading specimens which might affect the accuracy of the results. The cracking of the bending test specimens was more obvious than in the tensile test specimens, as they have a thicker size. However, it can be determined that the 65% vol solid loading will have a sintered specimen with less cracking than 60 vol% and 68 vol% solid loading. The flexural strength of the sintered specimens was gradually affected by the solid loading of the feedstock.

On the other hand, Figure 4.17 also shows that when varying the solvent used in solvent debinding, turpentine results in the highest average flexural strength of  $29.53 \pm 16.91$  MPa, followed by cyclohexane and n-heptane with an average flexural strength of  $27.79 \pm 13.19$  MPa and  $17.56 \pm 2.61$  MPa, respectively. This may be due to the fact that turpentine produces the least amount of minor cracks in the specimen compared to n-heptane and cyclohexane. Therefore, the choice of solvent used in solvent debinding will have a huge impact on the flexural strength of the sintered specimen.

Furthermore, Figure 4.17 shows that the flexural strength of the specimen increases from  $27.79 \pm 13.19$  MPa to  $43.41 \pm 3.52$  MPa when the raster angle changes from  $0^\circ/90^\circ$  to  $45^\circ/-45^\circ$ . This may be due to the fact that the crack pattern in the specimen mainly follows the raster. Thus, specimens with a  $0^\circ/90^\circ$  raster angle will have more cracking patterns parallel to the direction of force acting during the three-point bend test, resulting in lower flexural strength. Therefore, the raster angle will affect the flexural strength of the specimen.

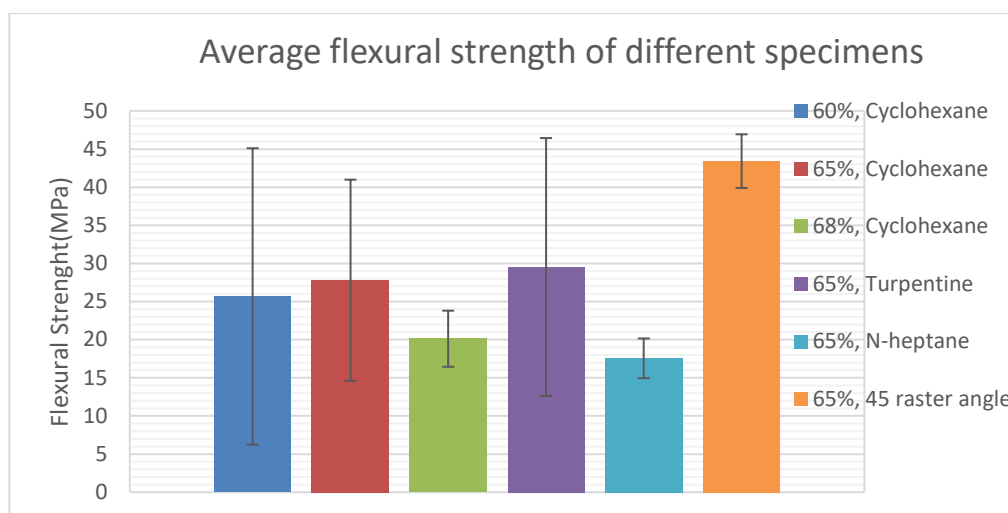


Figure 4.17: Bar chart of flexural strength of sintered specimen with different solid loading, debinding solvent and raster angle

### 4.7.3 Compressive Strength

Zirconia has been found to perform better in compressive tests due to its ability to close fractures and defects when crushed, preventing new cracks from developing (Huang, et al., 2021). In the compressive test, cylindrical sintered samples were tested until fracture. All types of specimens in Table 4.2, except for type six, were used in the compressive test as identical cylindrical specimens are produced when only varying the raster angle. The average compressive strength of the different types of sintered specimens calculated from the test results are shown in Figure 4.18.

In terms of solid loading, the average compressive strength decreases from  $844.19 \pm 140.61$  MPa to  $610.55 \pm 179.15$  MPa and  $550.76 \pm 23.36$  MPa when the solid loading increases from 60 vol% to 65 vol% and 68 vol%, respectively. This may be due to insufficient backbone binder to effectively hold the zirconia powder during printing, although an increase in solid loading can ensure the zirconia particles are packed closely and prevent voids in the sintered samples. The compressive strength of the sintered specimen is gradually affected by the solid loading of the feedstock.

In addition, when varying the solvent used in solvent debinding, Figure 4.18 shows the average compressive strength between cyclohexane, turpentine, and n-heptane. Turpentine resulted in the highest average compressive strength, followed by n-heptane and cyclohexane with values of  $847.58 \pm 313.75$  MPa,

798.19  $\pm$  140.47 MPa, and 610.55  $\pm$  179.15 MPa, respectively. The difference in average compressive strength may be due to turpentine and n-heptane resulting in a higher density than cyclohexane as a debinding solvent. Additionally, the average grain size of turpentine was the smallest compared to n-heptane and cyclohexane, which may also lead to higher compressive strength of the specimen. Therefore, the solvent used in solvent debinding will have a significant impact on the compressive strength, although it has no effect on the shrinkage and weight loss.

The effect of build orientation on average compressive strength was also examined in this research, comparing flat and on-edge orientations. As shown in Figure 4.18, the flat orientation resulted in a higher average compressive strength of 610.55  $\pm$  179.15 MPa compared to the on-edge orientation with 452.24  $\pm$  140.50 MPa. This difference in strength may be attributed to the porosity between layers in the printed samples, which is inherent in AM. Delamination, as observed in Appendix K, can occur more easily in cylindrical shapes when the build orientation is on-edge, resulting in a weaker structure and lower compressive strength. Thus, the build orientation of AM parts can significantly affect their compressive strength.

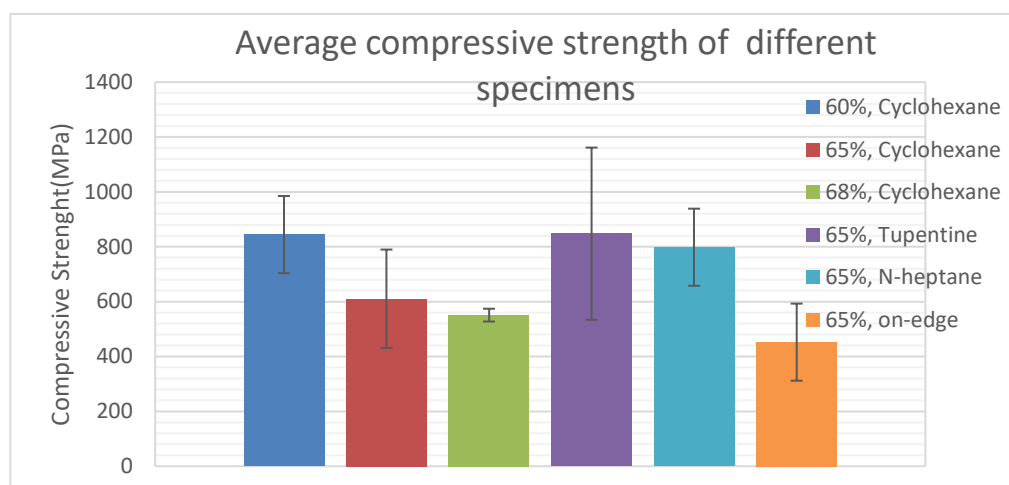


Figure 4.18: Bar chart of compressive strength of sintered specimen with different solid loading, debinding solvent and build-orientation

#### 4.7.4 Vickers Hardness

The sintered specimen, as shown in Appendix L. Specimen types one to five in Table 4.2 were used for the test, resulting in a total of 15 indentations from three different samples. Specimen types six and seven, which had different raster

angles and build orientations, were excluded from this test because recent research has shown that variation in printing parameters has no significant impact on the Vickers hardness of the specimens (Huang et al., 2021).

Figure 4.19 shows the average Vickers hardness of different specimens. The average Vickers hardness of the specimens increased from  $1123.13 \pm 155.82$  HV to  $1132.12 \pm 119.84$  HV and  $1191.21 \pm 91.27$  HV when the solid loading increased from 60 vol% to 65 vol% and 68 vol%, respectively. This may be due to the increasing solid loading causing the zirconia powder to pack closely during printing and sintering. Additionally, the grain size measured in Section 4.4 showed that 68 vol% had the smallest grain size when varying the solid loading, which might increase the Vickers hardness of the specimens. Thus, the higher the solid loading, the higher the Vickers number.

Additionally, Figure 4.19 shows the average Vickers hardness when the solvent used in solvent debinding was varied between cyclohexane, turpentine, and n-heptane. Turpentine resulted in the highest average Vickers hardness followed by n-heptane and cyclohexane with values of  $1228.82 \pm 35.45$  HV,  $1225.54 \pm 37.28$  HV, and  $1132.12 \pm 119.84$  HV, respectively. This may be due to the average grain size measured on sintered specimens that used turpentine as the debinding solvent, which was the smallest compared to n-heptane and cyclohexane. Thus, the smaller the grain size, the higher the Vickers hardness. Therefore, the Vickers hardness of the specimens will gradually be influenced by the solvent used in solvent debinding.

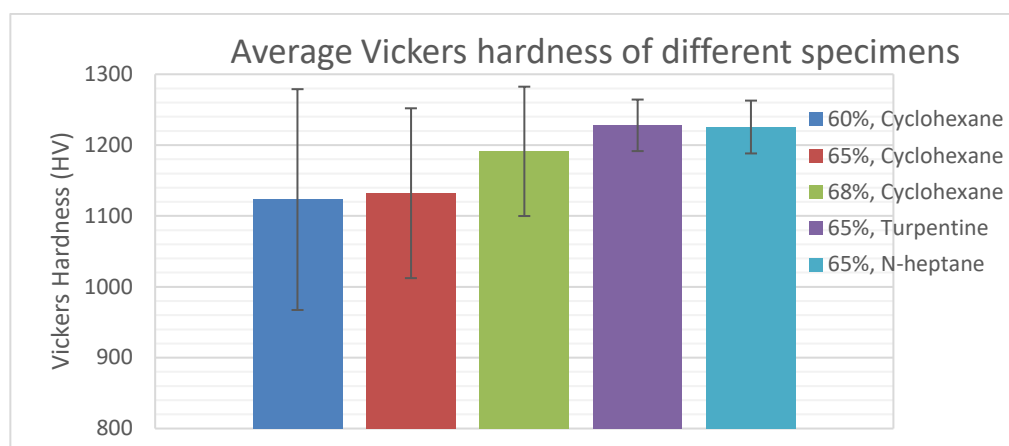


Figure 4.19: Bar chart of Vickers hardness of sintered specimen with different solid loading and debinding solvent



#### 4.8 Summary of Results

As the summary of results in this research, Table 4.4 shows the different feedstock's properties in term of thermal and rheological properties, Table 4.5 shows the grain size of different type of specimens, Table 4.6 shows the physical properties of specimens in term of shrinkage, weights loss, and density while Table 4.7 show the mechanical properties of specimens in term of flexural strength, compressive strength, and Vickers hardness with different solid loading, debinding solvent, raster angle, and build orientation.

Table 4.4: Table of Different Feedstock's Properties

Type of feedstock (solid loading)	60 vol%	65 vol%	68 vol%
Thermal properties			
Endothermic phase transition temperature	56 °C ~ 59 °C (PW and SA), 93 °C ~ 95 °C (LDPE)		
Binders decompose temperature	140 °C (PW and SA), 400 °C (LDPE)		
Complete decompose temperature	550 °C		
Amount of feedstock remaining	88.01 wt%	89.56 wt%	90.53 wt%
Rheological properties			
Newtonian or Non-Newtonian fluid	Non-Newtonian fluid, viscosity decrease when shear rate increase (shear thinning / pseudoplastic)		
Effect of temperature on viscosity	Temperature increase, viscosity decrease		
Viscosity	Relatively low	Moderate	Relatively high
Linear viscoelastic range (shear stain)	Below 0.1%		
Critical oscillatory strain (shear stain)	0.1%		
Shear yield strain (shear stain)	0.678%	0.314%	0.680%

Table 4.5: Table of Different Type of Sintered Specimen's Grain Size

Type of specimen	1	2	3	4	5
Solid loading	60 vol%	65 vol%	68 vol%	65 vol%	65 vol%
Debinding Solvent	Cyclohexane	Cyclohexane	Cyclohexane	Turpentine	N-heptane
Grain size (nm)	444 ± 27.2	444 ± 33.4	434 ± 20.7	426 ± 31.4	430 ± 25.4

Table 4.6: Table of Different Type of Sintered Specimen's Physical Properties

Type of specimen	1	2	3	4	5
Solid loading	60 vol%	65 vol%	68 vol%	65 vol%	65 vol%
Debinding Solvent	Cyclohexane	Cyclohexane	Cyclohexane	Turpentine	N-heptane
Sintered Shrinkage (%)	18.47 ± 0.92	16.71 ± 0.45	15.14 ± 0.62	16.73 ± 0.35	16.73 ± 0.45
Weight loss (%)	Solvent debinding				
	2.88 ± 0.88	2.32 ± 0.75	1.60 ± 0.44	2.38 ± 0.49	2.88 ± 0.64
	Sintered				
	12.08 ± 0.10	10.50 ± 0.13	9.76 ± 0.24	10.42 ± 0.13	10.49 ± 0.15
Density (g/cm <sup>3</sup> )	5.91 ± 0.05	5.85 ± 0.08	5.91 ± 0.07	5.89 ± 0.05	5.89 ± 0.04
Relative density (%)	97.33 ± 0.84	96.36 ± 1.32	97.30 ± 1.10	97.11 ± 0.81	97.11 ± 0.71

Table 4.7: Table of Different Type of Sintered Specimen's Mechanical Properties

Type of specimen	1	2	3	4	5	6	7
Solid loading	60 vol%	65 vol%	68 vol%	65 vol%	65 vol%	65 vol%	65 vol%
Debinding Solvent	Cyclohexane	Cyclohexane	Cyclohexane	Turpentine	N-heptane	Cyclohexane	Cyclohexane
Raster angle	0°/90°	0°/90°	0°/90°	0°/90°	0°/90°	45°/-45°	0°/90°
Build orientation	Flat	Flat	Flat	Flat	Flat	Flat	On-edge
Flexural Strength (MPa)	25.67 ± 19.44	29.53 ± 16.91	20.13 ± 3.68	29.53 ± 16.91	17.56 ± 2.61	43.41 ± 3.52	N/A
Compressive strength (MPa)	844.19 ± 140.61	610.55 ± 179.15	550.76 ± 23.36	847.58 ± 313.75	798.19 ± 140.47	N/A	452.24 ± 140.50
Vickers hardness (HV)	1123.13 ± 155.82	1132.12 ± 119.84	1191.21 ± 91.27	1228.82 ± 35.45	1225.54 ± 37.28	N/A	N/A

## CHAPTER 5

### CONCLUSIONS AND RECOMMENDATIONS

#### 5.1 Conclusions

All three types of feedstock exhibit shear thinning behaviour as their viscosity decreases with increasing shear rate. The viscosity of the feedstock decreases when the temperature was increased from 100 °C to 140 °C. The linear viscoelastic range of all three types of feedstocks was observed when the shear strain is below 0.1%, and the critical oscillatory strain was equal to 0.1%. Next, PW and LDPE started to decompose at around 140 °C and 400 °C, respectively.

In terms of physical properties, the dimension shrinkage decreased from 18.47% to 15.14% when the solid loading increased from 60 vol% to 68 vol%, while the debinding solvent had no effect on it. Moreover, the weight loss of the specimen decreased when the solid loading increased, while the debinding solvent had no effect on it. With regard to solid loading, 60 vol% solid loading gave the highest compressive strength of  $844.19 \pm 140.61$  MPa, while 65 vol% gave the highest flexural strength of  $29.53 \pm 16.91$  MPa, and 68 vol% solid loading gave the highest Vickers hardness of  $1191.21 \pm 91.27$  HV. Furthermore, turpentine performed the best among all the solvents (cyclohexane, turpentine, n-heptane) in terms of density, flexural and compressive strength, as well as Vickers hardness, with a value of  $5.89 \pm 0.05$  g/cm<sup>3</sup>,  $29.53 \pm 16.91$  MPa,  $847.58 \pm 313.75$  MPa, and  $1228.82 \pm 35.45$  HV, respectively. When the parameters were varied, 45°/-45° resulted in the highest flexural strength but the lowest tensile strength.

In addition, the grain size of the sintered specimen decreased slightly when the solid loading increased within the range of 444 nm to 434 nm. The grain size of the sintered specimen is also affected by the solvent used in solvent debinding, with turpentine resulting in the smallest grain size of 426 nm. Lastly, the sintered specimen had a tetragonal crystal structure that was not affected by solid loading and debinding solvent.

## **5.2 Recommendations for future work**

### **5.2.1 Prepare More Testing Sample for Tensile Test**

Recently, many tensile test samples were broken during gripping, making it impossible to conduct the test due to the brittle nature of ceramics, bending, and wrapping issues, even though these issues had been addressed by attaching two pieces of aluminum plates. Therefore, more samples should be prepared for each specimen and tested at least three times in order to obtain the average tensile strength of the sintered zirconia part.

### **5.2.2 Shorten The Time for Thermal Debinding**

The thermal debinding process used in this research took too long, about 3 days in total. This resulted in a small tolerance for error when preparing the specimens and limited the number of sintered samples that could be prepared during the final year project semester. Therefore, a shorter thermal debinding time would allow for more sintered specimens to be tested repeatedly, thereby increasing the accuracy of the results.

### **5.2.3 Using of Composite Backbone Binder**

Cracking frequently occurred during the preparation of the sintered specimens, which lowered the accuracy of the results. Therefore, a composite of backbone binder with high-density polyethylene and LDPE may be used to reduce cracking.

### **5.2.4 Explore More Solvent for Solvent Debinding**

This research shows that the debinding solvent can have a large impact on the quality of sintered samples in terms of density, grain size, flexural strength, compressive strength, and hardness. Therefore, it is crucial to explore more available solvents for solvent debinding, such as limonene, kerosene, and even combinations of turpentine and heptane, to determine the best solvent for solvent debinding.

## REFERENCES

- Arrigo, R. and Frache, A., 2022. FDM printability of PLA based-materials: the key role of the rheological behavior. *Polymers*, 14(9), p.1754.
- Dutrow, B.L and Clark, C.M, 2023. *X-ray Powder Diffraction (XRD)*. [online] Available at: <[https://serc.carleton.edu/research\\_education/geochemsheets/techniques/XRD.html](https://serc.carleton.edu/research_education/geochemsheets/techniques/XRD.html)> [Accessed 23 April 2023]
- Faes, M., Valkenaers, H., Vogeler, F., Vleugels, J. and Ferraris, E., 2015. Extrusion-based 3D printing of ceramic components. *Procedia Cirp*, 28, pp.76-81.
- He, Q., Jiang, J., Yang, X., Zhang, L., Zhou, Z., Zhong, Y. and Shen, Z., 2021. Additive manufacturing of dense zirconia ceramics by fused deposition modeling via screw extrusion. *Journal of the European Ceramic Society*, 41(1), pp.1033-1040.
- Huang, R., El Rassi, J., Kim, M., Jo, K.H., Lee, S.K., Morscher, G.N. and Choi, J.W., 2021. Material extrusion and sintering of binder-coated zirconia: comprehensive characterizations. *Additive Manufacturing*, 45, p.102073.
- Lakhdar, Y., Tuck, C., Binner, J., Terry, A. and Goodridge, R., 2021. Additive manufacturing of advanced ceramic materials. *Progress in Materials Science*, 116, p.100736.
- Li, H., Liu, Y., Liu, Y., Hu, K., Lu, Z. and Liang, J., 2020. Effects of Solvent Debinding on the Microstructure and Properties of 3D-Printed Alumina Ceramics. *ACS omega*, 5(42), pp.27455-27462.
- Liu, Z., Lei, Q. and Xing, S., 2019. Mechanical characteristics of wood, ceramic, metal and carbon fiber-based PLA composites fabricated by FDM. *Journal of Materials Research and Technology*, 8(5), pp.3741-3751.
- Masuda, H., Ohta, Y. and Kitayama, M., 2019. Additive manufacturing of SiC ceramics with complicated shapes using the FDM type 3D-printer. *Journal of Materials Science and Chemical Engineering*, 7(02), p.1.
- Matmatch, n.d. *Comparing Hardness Tests: Vickers, Rockwell, Brinell, Mohs, Shore and Knoop*. [online] Available at: <<https://matmatch.com/learn/process/hardness-comparison>> [Accessed 9 September 2022].
- Nötzel, D., Eickhoff, R. and Hanemann, T., 2018. Fused filament fabrication of small ceramic components. *Materials*, 11(8), p.1463.

- Pelz, J.S., Ku, N., Meyers, M.A. and Vargas-Gonzalez, L.R., 2021. Additive manufacturing of structural ceramics: a historical perspective. *Journal of materials research and technology*, 15, pp.670-695.
- Prabhu, R. and Devaraju, A., 2021. Recent review of tribology, rheology of biodegradable and FDM compatible polymers. *Materials Today: Proceedings*, 39, pp.781-788.
- RheoSense, n.d. *Viscosity of Newtonian and Non-Newtonian Fluids*. [online] Available at: <<https://www.rheosense.com/applications/viscosity/newtonian-non-newtonian>> [Accessed 9 September 2022].
- Saba, N., Jawaid, M. and Sultan, M.T.H., 2019. An overview of mechanical and physical testing of composite materials. *Mechanical and physical testing of biocomposites, fibre-reinforced composites and hybrid composites*, pp.1-12.
- Shaik, Y.P., Schuster, J. and Shaik, A., 2021. A Scientific Review on Various Pellet Extruders Used in 3D Printing FDM Processes. *Open Access Library Journal*, 8(8), pp.1-19.
- Solomon, I.J., Sevel, P. and Gunasekaran, J., 2021. A review on the various processing parameters in FDM. *Materials Today: Proceedings*, 37, pp.509-514.
- Swapp, S., 2017. *Scanning Electron Microscopy (SEM)*. [online] Available at: <[https://serc.carleton.edu/research\\_education/geochemsheets/techniques/SEM.html](https://serc.carleton.edu/research_education/geochemsheets/techniques/SEM.html)> [Accessed 23 April 2023]
- Witz, G., Shklover, V., Steurer, W., Bachegowda, S. and Bossmann, H.P., 2007. Phase evolution in yttria-stabilized zirconia thermal barrier coatings studied by rietveld refinement of X-ray powder diffraction patterns. *Journal of the American Ceramic Society*, 90(9), pp.2935-2940.
- Zhang, K., Xie, C., Wang, G., He, R., Ding, G., Wang, M., Dai, D. and Fang, D., 2019. High solid loading, low viscosity photosensitive Al<sub>2</sub>O<sub>3</sub> slurry for stereolithography based additive manufacturing. *Ceramics International*, 45(1), pp.203-208.

## APPENDICES

### Appendix A: Specification of Zirconia Powder

	Partially Stabilized Zirconia	
Grades	KZ-3YF type C	KZ-3YF type NF-S
	Powder characteristics	
Y <sub>2</sub> O <sub>3</sub> (wt%)	5.4	5.8
Al <sub>2</sub> O <sub>3</sub> (wt%)	0.25	0.25
Specific surface area(m <sup>2</sup> /g)	9	15
	Characteristics of sintered substance (at 1450°C)	
Sintered density(g/cm <sup>3</sup> )	6.07	6.07
Flexural strength (MPa)	1000	1000
Hardness(GPa)	12.5	12.5
Molding Methods	Injection, extrusion, and casting	Injection, extrusion

Figure A-1: Specification of Zirconia Dope with 3 mol% Yttria



## Appendix B: Feedstock Preparation



Figure B-1: Brabender Plastograph



Figure B-2: Feedstock with 60 vol% Zirconia, binder ratio LDPE: PW,  
40:60

## Appendix C: Detail Slicer Setting for Specimen Printing

**Layer height**

- Layer height:  mm
- First layer height:  mm

---

**Vertical shells**

- Perimeters:  (minimum)
- Spiral vase:

Recommended object thin wall thickness for layer height 0.30 and 2 lines: 0.74 mm , 3 lines: 1.07 mm , 4 lines: 1.41 mm

---

**Horizontal shells**

- Solid layers: Top:  Bottom:
- Minimum shell thickness: Top:  mm Bottom:  mm

Top shell is 0.9 mm thick for layer height 0.3 mm. Minimum top shell thickness is 0.21 mm.  
Bottom shell is 0.9 mm thick for layer height 0.3 mm. Minimum bottom shell thickness is 0.21 mm.

---

**Quality (slower slicing)**

- Extra perimeters if needed:
- Ensure vertical shell thickness:
- Avoid crossing perimeters:
- Avoid crossing perimeters - Max detour length:  mm or % (zero to disable)
- Detect thin walls:
- Thick bridges:
- Detect bridging perimeters:

---

**Infill**

- Fill density:  %
- Fill pattern:
- Length of the infill anchor:  mm or %
- Maximum length of the infill anchor:  mm or %
- Top fill pattern:
- Bottom fill pattern:

---

**Ironing**

- Enable ironing:
- Ironing Type:
- Flow rate:  %
- Spacing between ironing passes:  mm

---

**Reducing printing time**

- Combine infill every:  layers
- Only infill where needed:

---

**Advanced**

- Solid infill every:  layers
- Fill angle:  °
- Solid infill threshold area:  mm<sup>2</sup>
- Bridging angle:  °
- Only retract when crossing perimeters:
- Infill before perimeters:

---

**Skirt**

- Loops (minimum):
- Distance from brim/object:  mm
- Skirt height:  layers
- Draft shield:
- Minimal filament extrusion length:  mm

---

**Brim**

- Brim type:
- Brim width:  mm
- Brim separation gap:  mm

---

**Speed for print moves**

- Perimeters:  mm/s
- Small perimeters:  mm/s or %
- External perimeters:  mm/s or %
- Infill:  mm/s
- Solid infill:  mm/s or %
- Top solid infill:  mm/s or %
- Support material:  mm/s
- Support material interface:  mm/s or %
- Bridges:  mm/s
- Gap fill:  mm/s
- Ironing:  mm/s

---

**Speed for non-print moves**

- Travel:  mm/s
- Z travel:  mm/s

---

**Modifiers**

- First layer speed:  mm/s or %
- Speed of object first layer over raft interface:  mm/s or %

---

**Acceleration control (advanced)**

- Perimeters:  mm/s<sup>2</sup>
- Infill:  mm/s<sup>2</sup>
- Bridge:  mm/s<sup>2</sup>
- First layer:  mm/s<sup>2</sup>

---

**Extrusion width**

- Default extrusion width:  mm or %
- First layer:  mm or %
- Perimeters:  mm or %
- External perimeters:  mm or %
- Infill:  mm or %
- Solid infill:  mm or %
- Top solid infill:  mm or %
- Support material:  mm or %

---

**Overlap**

- Infill/perimeters overlap:  mm or %

---

**Flow**

- Bridge flow ratio:

---

**Slicing**

- Slice gap closing radius:  mm
- Slicing Mode:
- Slice resolution:  mm
- G-code resolution:  mm
- XY size Compensation:  mm
- Elephant foot compensation:  mm

---

**Other**

- Clip multi-part objects:

Figure C-1: Slicer Setting for Specimen Printing

## Appendix D: 3D Printer

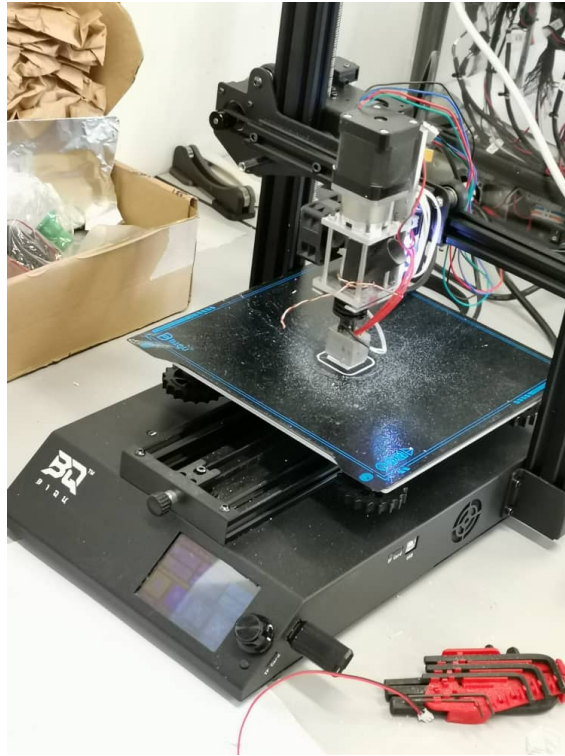


Figure B-1: Biqu B1 with customised extruder head

## Appendix E: Specimen for SEM



Figure E-1: Specimen after Grinding and Polishing



Figure E-2: Specimen Coated with Gold and Vanadium

## Appendix F: Printed, Debound and Sintered Sample

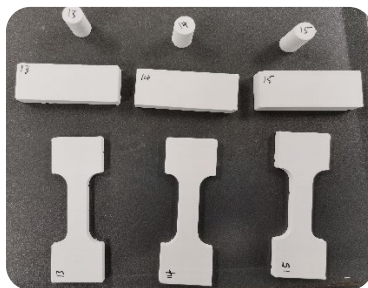


Figure F-1: Printed Sample



Figure F-2: After Solvent and Thermal Debinding Samples



Figure F-3: Sintered Samples

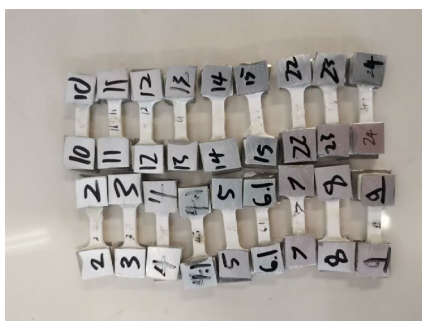


Figure F-4: Sintered Sample for Tensile Test



Figure F-5: Sintered Sample for Flexural Test



Figure F-6: Sintered Sample for Compressive Test

## Appendix G: Cracking of Sample

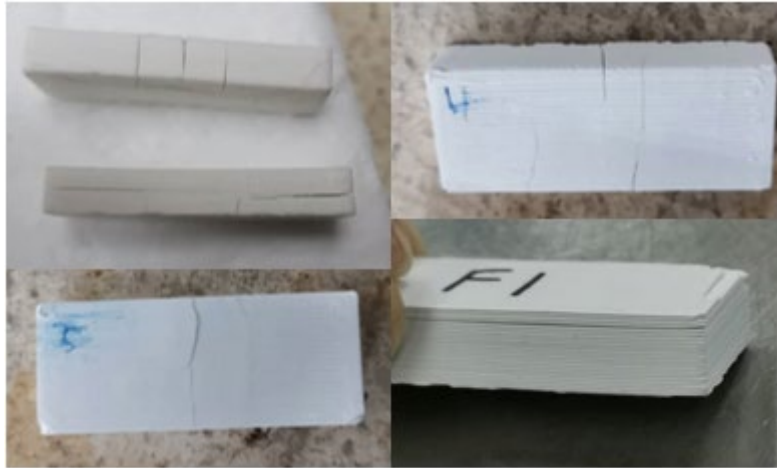


Figure G-1: Example of Cracking sample

## Appendix H: Fracture of Sample After Tensile Test

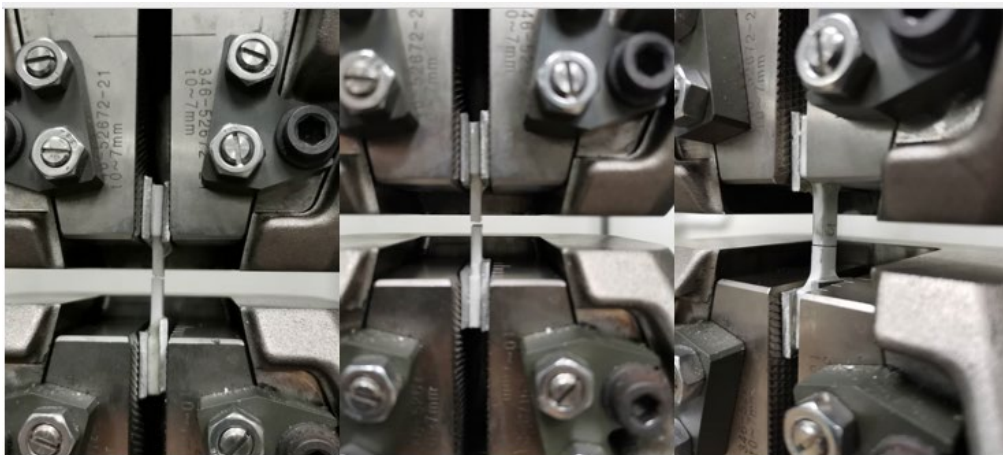


Figure H-1: Example of Conducting Tensile Test until Fracture



Appendix I: Tensile Test Specimen with Aluminum Plate

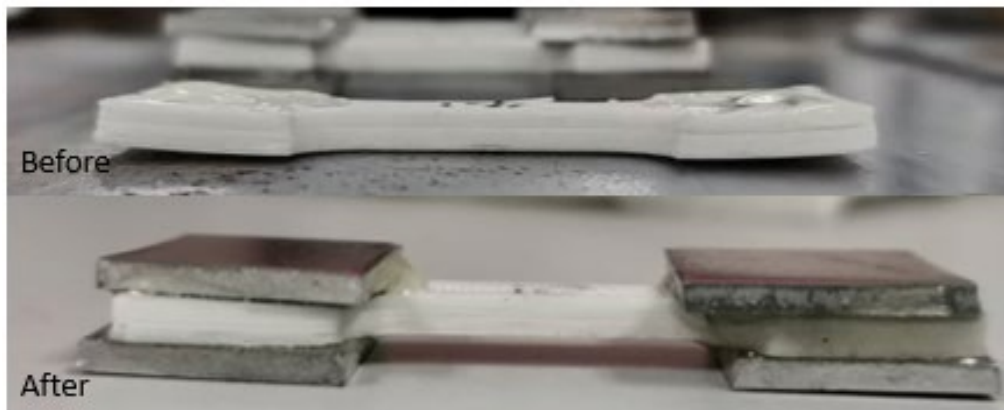


Figure I-1: Example of Before and After Adding of Aluminium Plate on Tensile Test Sample

Appendix J: Fracture of Sample After Three Point Bend Test

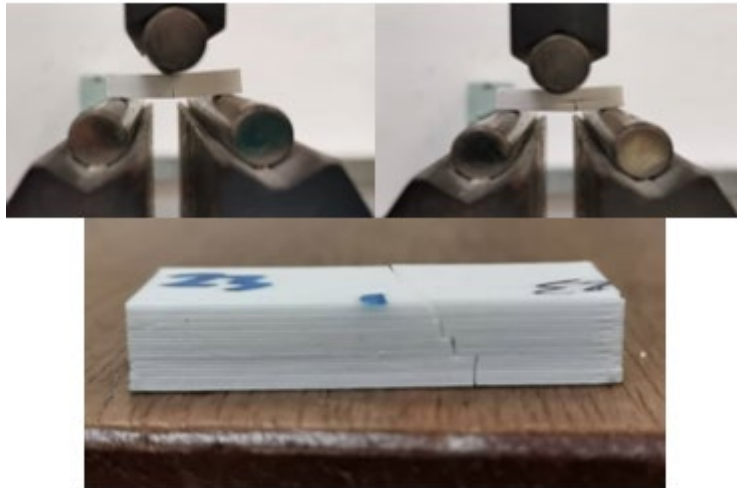


Figure J-1: Example of Conducting Three Point Bend Test until Fracture

## Appendix K: Delamination of Compressive Sample

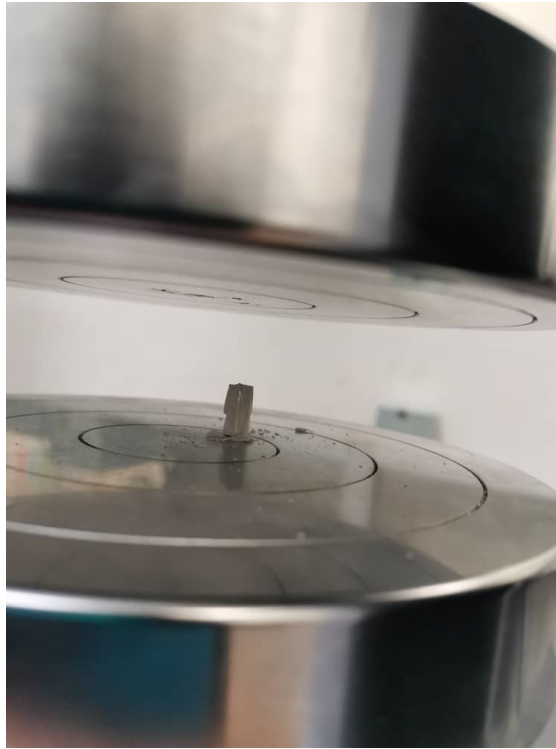


Figure K-1: Example of Delamination of Compressive Sample during Testing

Appendix L: Diamond Intend of Vickers Hardness Test

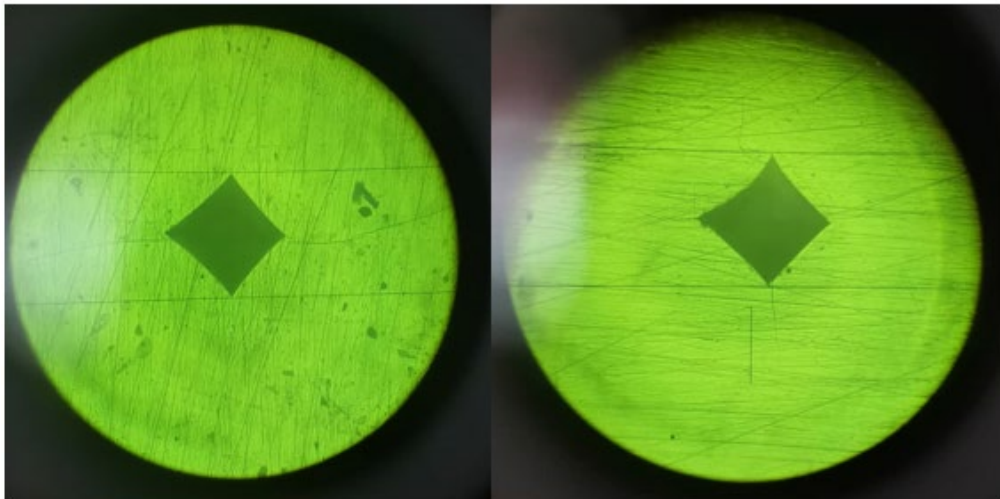


Figure L-1: Example of Diamond Shape Intend during Vickers Hardness Test